Groundwater

Convergence of Groundwater Discharge through the Hyporheic Zone of Streams

by Brian Babak Mojarrad[1] , Anders Wörman[2] , Joakim Riml[2] , and Shulan Xu[3]

Abstract

Significant attention has been given to hyporheic water fluxes induced by hydromorphologic processes in streambeds and the effects they have on stream ecology. However, the impact of hyporheic fluxes on regional groundwater flow discharge zones as well as the interaction of these flows are much less investigated. The groundwater-hyporheic interactive flow not only governs solute mass and heat transport in streams but also controls the retention of solute and contamination following the discharge of deep groundwater, such as naturally occurring solutes and leakage from geological waste disposal facilities. Here, we applied a physically based modeling approach combined with extensive hydrologic, geologic and geographical data to investigate the effect of hyporheic flow on groundwater discharge in the Krycklan catchment, located in a boreal landscape in Sweden. Regional groundwater modeling was conducted using COMSOL Multiphysics by considering geologic heterogeneity and infiltration constraint of the groundwater circulation intensity. Moreover, the hyporheic flow was analyzed using an exact spectral solution accounting for the fluctuating streambed topography and superimposed with the regional groundwater flow. By comparing the discharge flow fields with and without consideration of hyporheic flows, we found that the divergence of the discharge was substantially enhanced and the distribution of the travel times of groundwater was significantly shifted toward shorter times due to the presence of hyporheic flow. Particularly important is that the groundwater flow paths contract near the streambed interface due to the hyporheic flow, which leads to a phenomenon that we name "fragmentation" of coherent areas of groundwater upwelling in pinhole-shaped stream tubes.

Introduction

Heat and solutes can be generally introduced in streams by groundwater discharge that is generated by landscape topography over a wide range of scales, including large depths in bedrock. Investigations are conducted using biosphere models in which groundwater discharge through Quaternary deposits constitutes an important link for deep groundwater discharge into the surface environment (Hjerpe and Broed 2010; Saetre 2015). The

[1]Corresponding author: Department of Sustainable Development, Environmental Science and Engineering, KTH Royal Institute of Technology, Stockholm 100 44, Sweden; mojarrad@kth.se

[2]Department of Sustainable Development, Environmental Science and Engineering, KTH Royal Institute of Technology, Stockholm, 100 44, Sweden

[3]Xu Environmental Consulting AB, Stockholm, 168 61, Sweden

residence time of groundwater in Quaternary deposits can be used to parameterize compartment models to analyze solute and contaminant transport in the biosphere and geosphere environments.

The groundwater flow in the relatively thin Quaternary deposits in Scandinavia hydrologically behaves quite differently from the bedrock flow due to variations in hydraulic conductivity and porosity, which therefore causes an abrupt reduction in the groundwater discharge velocity close to the surface water interface. In addition, the solute travel times will be relatively longer in the soil layer than in surface water, and solute and contaminant can accumulate in soil due to adsorption and consequently contaminate future agricultural products (Berglund et al. 2009; Kautsky et al. 2013). In particular, streambed sediments act as regulators of stream water quality and ecosystems and, hence, can strongly influence the health of humans and other biota. Solute elements, such as ^{222}Rn, and temperature have been used as tracers to identify groundwater flows from different depths separated from stream hyporheic flows. By using such tracers, one can assess the discharge locations of deep groundwater and the contribution of discharge to stream flows (Dimova and Burnett 2011).

Several studies have considered the impact of groundwater discharge on hyporheic flow (Boano et al. 2008; Fleckenstein et al. 2010; Bhaskar et al. 2012; Trauth

et al. 2014; Hassan et al. 2015; Fox et al. 2016), but only a few studies have considered the reverse effect of hyporheic flow on groundwater discharge. Many of previous studies did not consider the hierarchically nested structure of the groundwater flow structure on a regional scale, but an exception is the study of Caruso et al. (2016). In addition, previous research on solute and contaminant transport in groundwater did not specifically consider the flow interaction of surface water and groundwater (Wörman et al. 2007a; Selroos and Painter 2012). From combined observations of water quality and temperature, it has been concluded that groundwater discharge zones often form rather small stream areas receiving water from manifold larger catchment areas; such areas have lately been termed discrete riparian inflow points (DRIPs) (Ploum et al. 2018, 2021), but the phenomenon of concentrated groundwater inflow in streams has been well known for decades (Jansson et al. 2007; Schuetz and Weiler 2011; Kuglerová et al. 2014).

This study focuses on the geohydrologic-hydromechanical explanation of a similar phenomenon arising due to the large-scale groundwater circulation and its interaction with the more intense flow in stream beds. In the scientific literature, we find that the ratio of regional groundwater to hyporheic flow velocities could be in the range of 10^{-2} to 10^{-4} (Bhaskar et al. 2012; Gomez-Velez et al. 2014), which indicates that hyporheic flow is generally much more intense than groundwater discharge and, therefore, should have a significant effect on narrowing the discharge zones. In particular, hyporheic flows may have implications, which could be important for further transport of discharging solutes in surface water (Xu et al. 2008).

This study is focused on the relative importance of hyporheic flow on upwelling groundwater with application to the Krycklan catchment, which is located in a boreal landscape in Sweden. The aim is to use a mathematical modeling framework to study the relative effects of hyporheic flows on the discharge of groundwater and, especially, to constrain the model framework with extensive field data on hydrology, geology, physical geography and topography. To represent the wide range of spatial topographical scales of importance, we propose a separate treatment of hyporheic and regional groundwater flows. Hence, a general approach is to mathematically superimpose the hyporheic and regional groundwater flows, particularly in identified discharge zones, hence facilitating a detailed study of effects on the hyporheic flow in discharge of deep upwelling groundwater. A hypothesis is that many factors, such as landscape topography, geology, and climate, control hyporheic flows and groundwater discharge and that the interaction of these flows is important to the discharge phenomenon.

A modeling framework similar to that used here was introduced by Mojarrad et al. (2019b), but this study develops the model substantially with respect to geologic heterogeneity and hydrologic constraints due to groundwater infiltration and renewal rates. The latter is of utmost importance to the overall intensity of groundwater

circulation and hence to the discharge intensity. Major developments comprise (1) the application of more constraints due to observations of soil and bedrock type and associated heterogeneity of hydraulic conductivity, groundwater infiltration, landscape topography and specific hydraulic conductivity values for the hyporheic zone, (2) particle tracing for assessing the behavior of deep groundwater from large depths in bedrock to discharge zones, and (3) the geologic layering of the model into three units representing sediments, Quaternary deposits, and bedrock. A Monte Carlo analysis is suggested to cover uncertainties in the mathematical simulations of hyporheic flows. All these developments were considered essential to the aims of the study focused on analyzing the relative importance of streambed-induced hyporheic flow on deep groundwater discharge.

Methodology

Empirical and Observational Data

The study was performed using data from the Krycklan catchment, which is located in northern Sweden near the city of Umeå (64°14′ N, 19°46′ E). Krycklan is a research catchment with a 68-km² area and extensive field infrastructure for monitoring hydrology, water quality, stream biodiversity, and climatology (Laudon et al. 2013). The catchment consists of 15 subcatchments that are instrumented for discharge measurements (Figure 1). The measured stream discharges along with the physical characteristics of the stream network were used to quantify the streambed-induced flow field (Section "Streambed-Induced (Hyporheic) Flow"). High-resolution topographic digital elevation data exist for the entire catchment; in these data, the horizontal and vertical resolutions are 2 m and 1 cm, respectively. The catchment elevation is in the range of 117 to 405 m above sea level. Bedrock surface elevation data with a horizontal resolution of 10 m were provided by ©Sveriges geologiska undersökning (SGU). The thickness of the Quaternary deposits was quantified by subtracting the bedrock surface elevation from the topographic digital elevation data.

The Krycklan landscape was formed during the last glaciation (Lidman et al. 2016); the northern part primarily consists of a 15 to 20 m thick glacial till. The glacial till intertwines with regions containing peat and/or lake sediment toward the east. The glacial till mainly contains basal till in the deep soil, which is replaced with ablation till in the shallow soil (Jutebring Sterte et al. 2021). The southern side of the Krycklan catchment has a lower elevation compared with other regions, where the soil is a mixture of fluvial and glaciofluvial deposits. These regions mainly consist of sandy and silty sediments with significant soil thickness (i.e., approximately 40 m deep), where the soil has been compacted by its own weight (Lyon et al. 2011). Generally, the aggregates of till soil shrink with depth, and in sandy silty sediment, sand is replaced with silty clay as the depth increases. In addition, peat is replaced with clay within a few meters of the

NGWA.org

B.B. Mojarrad et al. Groundwater 61, no. 1: 66–85 67
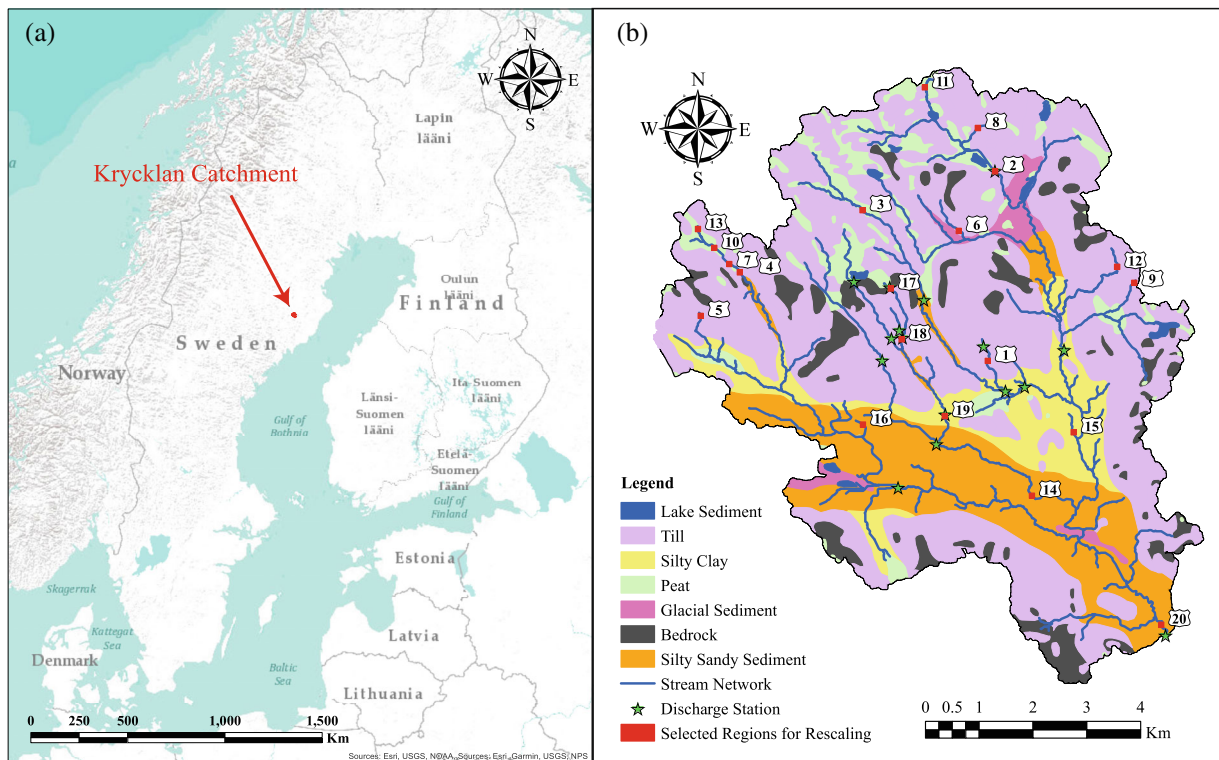
Figure 1. (a) Map showing the location of the Krycklan catchment in Sweden, and **(b)** map showing the soil types of the Krycklan catchment, as well as the stream network (blue lines) and the discharge stations (green stars) within the catchment. Moreover, the positions of the selected 100 m × 100 m regions for rescaling the local streambed topography (red squares) used in the streambed-induced model are also shown. The labels correspond to selected 100 m × 100 m regions that were used as the topographic realization in streambed-scale modeling.

surface (Sterte et al. 2018). The soil type data are available at the Krycklan catchment website (https://www.slu.se/krycklan). Seven different soil types exist in the Krycklan catchment (Figure 1), and the hydraulic conductivity of each soil type was obtained by Sterte et al. (2018) to reflect heterogeneities in the Quaternary deposits.

The streambed sediment was defined as the top 5 m of soil beneath the stream network (with a 5-m width) in which a hydraulic conductivity of 9.13×10^{-4} m/s was considered at the streambed interface, as obtained from an experiment by Morén et al. (2017) (Section "Regional-Scale Groundwater Flow Numerical Modeling"). In addition, hydraulic conductivity was considered to exponentially decay with depth. The mean annual precipitation (from 1981 to 2010) was estimated to be 726 mm by the ©Swedish Meteorological and Hydrological Institute, SMHI. Considering the forestry type of the Krycklan catchment containing dense trees and bushes, the average annual infiltration rate was assumed to be a function of effective precipitation (precipitation rate minus evapotranspiration rate). Hence, the estimated mean annual runoff provided by the SMHI was set as the infiltration rate (i.e., 382 mm/year). Steady state modeling allowed the use of infiltration as the catchment-scale constraint so that the mean value of the vertical flux at the top surface of the catchment-scale model did not exceed the mean infiltration value. This constraint was fulfilled

by using the variable resolution of the topographic elevation data (Section "Regional-Scale Groundwater Flow Numerical Modeling").

Modeling Framework

A steady-state multiscale modeling framework was applied in this study to cover the spectrum of scales affecting the interactions between the groundwater and surface water that occur within streambed sediments. Similar to the work of Mojarrad et al. (2019b), the flow problem was addressed at two spatial scales: the catchment scale and streambed scale. The catchment scale groundwater flow was numerically modeled with a combination of topography- and recharge-controlled boundary conditions of the top surface; whereas the streambed scale (hyporheic) flow was modeled via exact solutions bounded with streamflow characteristics on the top (Section "Regional-Scale Groundwater Flow Numerical Modeling" and "Streambed-Induced (Hyporheic) Flow").

At the catchment scale, the model was constrained by data representing the landscape topography, geological heterogeneity of both the Quaternary deposits and bedrock, stream network extension and the mean annual infiltration rate controlling the overall circulation intensity of the groundwater (Section "Empirical and Observational Data" for data description). The momentum equation for subsurface flow in saturated porous media at a sufficiently

low Reynolds number is generally derived by neglecting inertia terms while maintaining the potential energy and adopting a linear friction-loss relationship. This leads to the well-known Darcy's law: $\mathbf{q}\,(u, v, w) = -K\nabla H$. Here, K (m/s) is the hydraulic conductivity, ∇ is the nabla operator, H (m) is the total hydraulic head, q (m/s) is the Darcy velocity vector, and u (m/s), v (m/s), and w (m/s) are Darcy's velocities in the x, y, and z directions, respectively, while bold symbols denote vector quantities (Whitaker 1986). The application of Darcy's law in the three-dimensional (3D) steady-state groundwater flow equation is described as follows:

$$\frac{\partial}{\partial x}\left(-K_x\frac{\partial H}{\partial x}\right) + \frac{\partial}{\partial y}\left(-K_y\frac{\partial H}{\partial y}\right) + \frac{\partial}{\partial z}\left(-K_z\frac{\partial H}{\partial z}\right) = 0 \tag{1}$$

where $H = z_e + p/(\rho \times g)$; z_e (m) is the elevation; p (Pa) is the pressure; g (m/s^2) is the acceleration due to gravity; and ρ (kg/m^3) is the water density. Moreover, x (m), y (m), and z (m) are the spatial directions, among which x and y lie on the horizontal surface and z represents the vertical spatial direction (positive upward). Since Equation 1 is a linear function, the superposition principle can be used to separate the total hydraulic head, $H(x,y,z)$ (m), into individual terms operating on different spatial scales, as follows:

$$H(x, y, z) = H_S(x, y, z) + H_C(x, y, z) \tag{2}$$

where H_S (m) is the streambed-induced hydraulic head fluctuation and H_C (m) is the catchment-scale hydraulic head. The catchment-scale hydraulic head reflects the trend and fluctuation in the catchment-scale water surface elevation, whereas the streambed-induced hydraulic head can be regarded as a local detrended perturbation of the water surface along the streams and lakes. In this study, the catchment scale was modeled using numerical solutions (Section "Regional-Scale Groundwater Flow Numerical Modeling"). However, an exact solution was used to represent H_S for streambed-induced flow modeling (Section "Streambed-Induced (Hyporheic) Flow"). The mean of the absolute value of Darcy's vertical velocity of the catchment scale model at $z = z'$ is evaluated as follows:

$$\langle|W_C|\rangle = \frac{1}{A_z}\int_{A_z}\left(\left|W\left(x, y, z = z'\right)\right|\right)\,dA_z \tag{3}$$

where W_C (m/s) is Darcy's velocity in the z direction, A_z (m^2) is the surface area, z' (m) is any arbitrary depth, and d is the differential operator. Darcy's velocity is defined as the flow velocity averaged over the entire cross-sectional area of a porous medium. However, the seepage velocity (also called the pore water velocity) is defined as $v_{seepage} = q/n$. Thus, $v_{seepage}$ (m/s) is the flow velocity divided by the porosity of the media, n $(-)$, and is representative of the transport time of inert water in groundwater. Solute retardation was added to estimate the solute transport time in different subsurface strata. In

this study, the retardation of the ^{135}Cs transport time in different layers was evaluated using $t_{solutes} = (1 + R) \times t_{water}$, where t (s) is the transport time and R $(-)$ is the retardation factor for each subsurface stratum due to sorption and diffusion processes. It should be noted that t_{water} corresponds to the travel time of water, estimated by the seepage velocity. The values used for the retardation factor in rock fractures, as well as in Quaternary deposits and sediments, were $R_{rock} = 10$ and $R_{QD,sediment} = 500$ (Jakubick 1979; Neretnieks 1979; Wörman et al. 2004).

Regional–Scale Groundwater Flow Numerical Modeling

The catchment-scale numerical model was conducted in COMSOL Multiphysics®. The bounding rectangle of the Krycklan catchment (i.e., 11.6 km × 10.3 km) was set as the horizontal limit of the numerical model's domain (64°11.8′ N to 64°17.6′ N, 19°39.5′ E to 19°54.3′ E). The entire domain was stratified into three volume units representing streambed sediments, Quaternary deposits, and bedrock where each unit divided into several layers in the applied finite element method. Here, the streambed sediment was defined as the top five meters of Quaternary deposits along the stream network, while the full thickness of the Quaternary deposits (sediments and underlying soil strata) was obtained through analysis of the soil depth data. However, the streambed sediment unit was removed from the numerical model where bedrock outcrops existed.

Previous studies have shown that hydraulic conductivity decays with depth for most geological units (Ingebritsen and Manning 1999; Saar and Manga 2004; Ryan and Boufadel 2007; Jiang et al. 2009; Grant et al. 2014; Ameli et al. 2016a). In particular, Ameli et al. (2016b) used a semi-analytical approach to determine the depth-decaying hydraulic conductivity in the Krycklan catchment. Hence, the hydraulic conductivity of each individual unit is described according to an exponential function that reflects a decreasing decay with depth in all media, as follows:

$$K_i(z) = K_{(S \text{ or } QD \text{ or } B),top}\, e^{\frac{(z-z_{top,i})}{\delta_i}} \tag{4}$$

where the subscript i represents the different units; $K_{S,top}$ (m/s), $K_{QD,top}$ (m/s), and $K_{B,top}$ (m/s) are the hydraulic conductivities at the top surfaces of the streambed sediment (S), Quaternary deposit (QD), and bedrock (B) units, respectively; $z_{top,i}$ (m) is the elevation at the top surface of the corresponding unit; and δ (m) is the skin depth. Saar and Manga (2004) indicated that the skin depth varies in the range of 200 to 300 m for both Quaternary deposits and bedrock. In the present study, we considered $\delta = 250$ m for the Quaternary deposit and bedrock units. Furthermore, $1/\delta$ is an empirical decay coefficient for streambed sediments that can be determined experimentally (Marklund and Wörman 2011). In this study, the decay coefficient of the streambed sediment unit was calculated based on the depth-varying hydraulic conductivity observations reported by Morén et al. (2017) (Figure S1, supporting information).
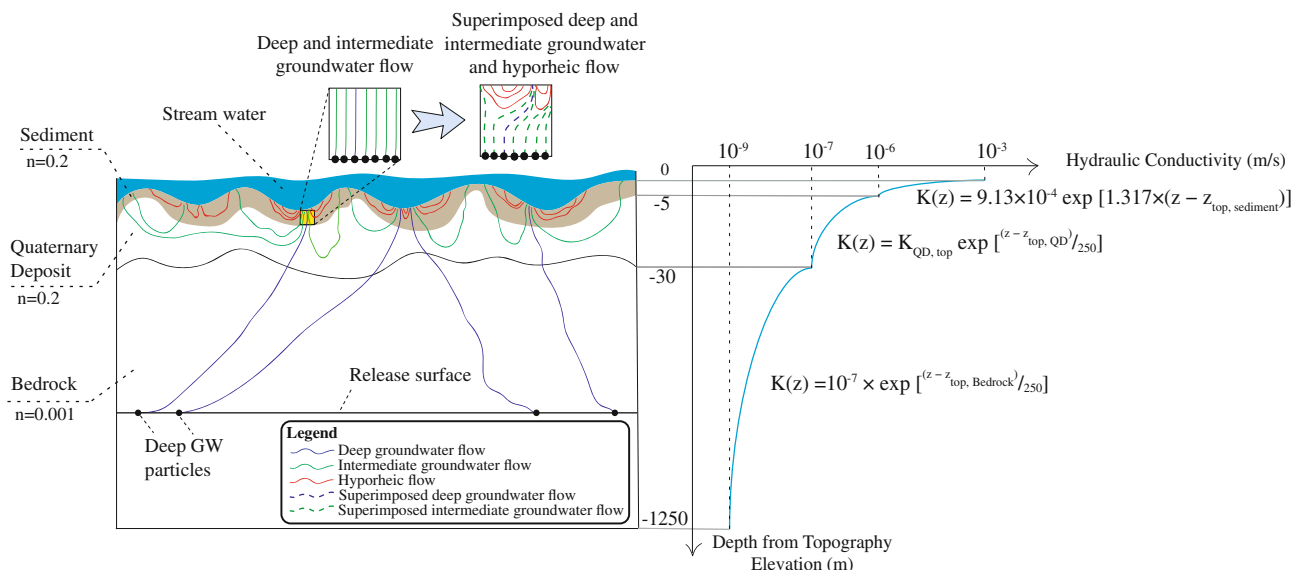
Figure 2. Schematic sketch of the considered porosity, n, and depth-decaying hydraulic conductivity, K, in the three different layers of the model. Note that the axes are not to scale. In addition, the multiscale flow processes that are accounted for in the present study are shown with a schematic cross-sectional sketch. The catchment-scale model only covers the deep and intermediate groundwater flow fields (blue and green solid lines, respectively), while the streambed-scale model evaluates the hyporheic fluxes (red solid lines). The superimposed deep and intermediate flows (blue and green dashed lines, respectively) are influenced by the hyporheic fluxes. Note that the figure is not to scale.

Additionally, the heterogeneity in the hydraulic conductivity of the Quaternary deposits (K_{QD}) was considered using a soil map and the associated hydraulic conductivity patterns over the Krycklan catchment (Sterte et al. 2018). The bedrock unit was considered as a continuum, where the hydraulic conductivity is represented by an averaged value for a mixture of both the intact bedrock and fracture network. In addition, the hydraulic conductivity of the crystalline bedrock continuum was considered to decay exponentially using Equation 4, where the hydraulic conductivity of the top surface of the bedrock unit was chosen to be 1×10^{-7} m/s based on the values provided by Ericsson et al. (2006). Macroscopic variation of the (continuum) hydraulic conductivity was disregarded because no major fracture zones are known to pass the investigated area. The porosity of the bedrock unit was assumed to be 0.001, whereas the porosities of the Quaternary deposits and sediment units were assumed to be 0.2 (Figure 2).

The mesh sizes varied both horizontally and vertically within the ranges of 0.1 to 2 m, 2 to 17 m, and 17 to 403 m for the streambed sediment, Quaternary deposit, and bedrock units, respectively. In addition, the maximum element growth rate and the curvature factor for the streambed sediment are 1.15 and 0.1, respectively, while these change to 1.2 and 0.2 for Quaternary deposits and 1.35 and 0.3 for streambed sediment, respectively. The water table in the Krycklan catchment was classified as topography-controlled, which reflects that the water table is a subdued, smoothed replica of the elevation of the landscape (Mojarrad et al. 2019b). However, the correlation between the fluctuating topography and groundwater level may spatially vary due to the impact of infiltration (Haitjema and Mitchell-Bruker 2005). In particular, topography has a controlling local impact on the water level where surface water resources exist, whereas infiltration plays a major role in terrain with high local elevations (Sanford 2002; Bresciani et al. 2016a, 2016b). Hence, the realistic condition is to set topography-controlled boundary conditions (i.e., Dirichlet) at lakes and streams while setting a recharge-controlled boundary condition (i.e., Neumann) for the rest of the terrain. Dirichlet boundary condition represents the specified head boundaries at water resources objects such as lakes and streams, whereas Neumann boundary condition reflects specified flux boundaries representing the infiltration from the precipitation.

Previous studies have indicated that the resolution of the chosen digital elevation model (DEM) strongly affects the vertical groundwater flux at the topographic surface, that is, infiltration or groundwater recharge (Marklund and Wörman 2011; Wang et al. 2018). Therefore, the top boundary condition of the numerical model was aligned with the landscape topographic elevation but was smoothed by changing the DEM resolution over (only) the recharge areas to constrain the recharge rate to the observed infiltration of the catchment. The applied method implies that the numerical solution is formally derived using a constant head (Dirichlet boundary condition) at the groundwater table, but the smoothed boundary also satisfies limited infiltration (Neumann boundary condition). The smoothing of the groundwater table was performed by lowering the resolution of the mesh size of the identified recharge areas via an iterative mesh approach until the annual infiltration rate of the catchment was satisfied.

No flow boundary condition was assumed for the flat horizontal surface at the bottom of the model. Additionally, the total depth of the domain, D_T, varied spatially within the catchment, ranging from 950 to 1250 m depending on the surface elevation. In addition, the impact of the sides of the numerical model was accounted for by applying a constant hydraulic head to the vertical surfaces of the rectangular domain ($H_C(x, y, z)|_{x=0,L_x \text{ and } y=0,L_y} = Z_B(x, y)$, where $Z_B(x,y)$ is the landscape topographic elevation and L_x and L_y represent the lengths of the catchment in the x and y directions, respectively).

Streambed–Induced (Hyporheic) Flow

To superimpose the results of the analyses of hyporheic flow onto the regional groundwater flow, at the top boundary of the hyporheic flow domain, we only recognized the local fluctuations of the streambed hydraulic head from the regional hydraulic head. Hence, the fluctuations of the streambed hydraulic head were applied as a boundary condition for the hyporheic flow, that is, the flow of surface water through streambed sediment inflow paths that re-emerges into surface water. The hyporheic flow model was analyzed at all points within the catchment boundaries where discharge from deep groundwater was found (Section "Spatial Representativity of the Streambed-Induced Flow"). These areas were used to determine the effect of hyporheic flow on the discharge of groundwater.

A hyporheic flow can be decomposed into hydrostatic and dynamic components that are both induced by the streambed topography. Here, the hydrostatic head component is conceived as the water-surface elevation, whereas the dynamic head component is defined as the deviating pressure variation at the sediment-water interface that varies due to the acceleration of flowing water over bedforms (i.e., the conversion of velocity head into a pressure head). Following Mojarrad et al. (2019b) and Marklund and Wörman (2011), the streambed-induced hydraulic head with an exponentially depth-decaying hydraulic conductivity can be represented as follows:

$$H_S(x, y, z) = \sum_{j=1}^{N}\sum_{i=1}^{N}\left[C_{damp}(\lambda_i) + \left(\frac{h_m}{\sigma_{S,B}\sqrt{2}}\right)\right]$$
$$(A)_{i,j}\sin(k_i x)\cos(k_j y) \times e^{-\left(-\frac{c}{2}+\sqrt{\frac{c^2}{4}+\alpha\left(k_x^2+k_y^2\right)}\right)z}$$
(5)

where N (−) refers to the number of wavelengths, $(A)_{i,j}$ (m) are amplitude coefficients determined from the local streambed topographic elevation, $(A)_{i,j}\sin(k_i x)\cos(k_j y)$; $k = 2\pi/\lambda$ (m^{-1}) is the wavenumber, λ (m) is the wavelength, c (m^{-1}) is an empirical decay coefficient, $\alpha = (K\_x \text{ or } K\_y)/K\_z$ (−) is the anisotropy ratio, and $C_{damp}(\lambda)$ is the hydrostatic damping factor representing the smoothness of the water surface in comparison to the streambed surface, which has been shown to be a function of wavelength (Morén et al. 2017). Furthermore, $(h\_m/(\sigma\_(S, B)\sqrt{2}))$

is the dynamic head coefficient, in which h_m (m) and $\sigma_{S,B}$ (m) are the amplitude corresponding to the velocity head deviation and the standard deviation of the streambed topography elevation, respectively, both evaluated along the stream channel and, thus, constants within each topographic realization representing the streambed scale. Fehlman (1985) defined an equation for estimating the amplitude of the velocity head variation for a two-dimensional, solid, triangular bedform shape ($Z\_BM/\lambda = 1/7$, in which Z_{BM} (m) is the bedform height; Elliott and Brooks 1997a, 1997b):

$$h_m = 0.28\left(\frac{v_f^2}{2\,g}\right)\begin{cases}\left(\frac{Z_{BM}/D_w}{0.34}\right)^{3/8} & Z_{BM}/D_w \leq 0.34 \\ \left(\frac{Z_{BM}/D_w}{0.34}\right)^{3/2} & Z_{BM}/D_w \geq 0.34\end{cases}$$
(6)

where v_f (m/s) is the average flow velocity in the stream, g (m/s^2) is the gravitational acceleration, and D_w (m) is the flow depth. Later, Stonedahl et al. (2010) extended Fehlman's equation to be applicable for sinusoidal bedforms with an amplitude of $Z_{BM} = 2\sqrt{2}\sigma_{S,B}$, which was used in this study.

The topography of the landscape and the streambeds have been shown to follow fractal patterns, allowing a spectral representation of the head boundary condition, as well as 3D solutions to topography-controlled groundwater circulation (Wörman et al. 2006, 2007b). The fractality reflects a constant power law correlation between the topographic amplitude and wavelength across all scales in a real Fourier series representing the topographic elevation. This fractal power has been shown to prevail over a wide range of scales, from continental scales to bedforms in streams (Wörman et al. 2007a), suggesting that there is a possibility of extrapolating streambed surface topography over scales for which high-resolution streambed topographic data are not available. Previously, methods for rescaling observed landscape topography to smaller scales to generate streambed topography have been applied (Morén et al. 2017; Mojarrad et al. 2019b). Here, a similar rescaling method was utilized, using landscape topography with a size of $100\,\text{m} \times 100\,\text{m}$ and a resolution of $2\,\text{m} \times 2\,\text{m}$ identified on a DEM of the topography surrounding the stream. These regions were rescaled to a size of $5\,\text{m} \times 5\,\text{m}$ and a resolution of $0.1\,\text{m} \times 0.1\,\text{m}$ to represent the streambed topography. It should be noted that the size of streambed topography and the resolution of this streambed domain correspond to a length scale representative to the depth of flow in the hyporheic zone (Morén et al. 2017). The details of the rescaling process are described in Mojarrad et al. (2019b).

Although the hyporheic flow solution according to Equation 5 applies to a domain of infinite extent in the x-, y- and z-directions, the hyporheic flow was represented using $5\,\text{m} \times 5\,\text{m} \times 5\,\text{m}$ extracted from the flow field using discharge points of the deep groundwater. In addition, the hydraulic conductivity of the hyporheic-scale model was determined via Equation 4 (i.e., similar to the streambed sediment unit of the regional-scale model).

NGWA.org

B.B. Mojarrad et al. Groundwater 61, no. 1: 66–85   71

Spatial Representativity of the Streambed–Induced Flow

This study recognized uncertainties in the hydrostatic and dynamic head boundary conditions by performing a sensitivity analysis on the parameters in Equation 5, while the uncertainty in the other parameters of the hyporheic flow model (such as hydraulic conductivity, and so on) and in those of the catchment-scale flow model was not formally analyzed. Due to the uncertainty in the hydrostatic damping factor and dynamic head coefficient, a Monte Carlo sensitivity analysis was conducted to provide a statistically representative sampling of the possible streambed-induced flow fields. The hydrostatic damping factor reflects the ratio of the water surface to bedform variations and ranges between 0 and 1. In addition, the streambed-induced dynamic head coefficient depends on the flow velocity, flow depth, and variation in the bedform elevation (Equation 6). Since the aim of the study was to investigate the impact of hyporheic fluxes on deep groundwater discharge zones, the stream flow velocity and flow depth of the hyporheic dynamic head coefficient should be representative of the deep groundwater discharge points along the stream-lake network. Hence, the catchment-scale groundwater flow discharge points were clustered into 30 different subcatchments (based on the deep groundwater discharge locations at the topographic surface) to represent a broad range of stream flow characteristics within the study area. Then, the flow velocity and water depth were estimated for each subcatchment based on the corresponding drainage areas and mean values of the physical characteristics of the stream segments identified for each of the subcatchments (Table S1 and Figure S2 in the supporting information). Consequently, the deep groundwater discharge points at the topographic surface that were grouped together were assumed to have the same flow velocity and flow depth values in the streambed-scale model.

Equation 5 shows the impact of streambed topographic elevation, $(A)_{i,j} \sin(k_i x) \cos(k_j y)$, on the hyporheic flow hydraulic head given a specific hydrostatic damping factor and dynamic head coefficient.

Hence, 20 arbitrary landscape topographies were selected (red squares in Figure 1b) and rescaled to streambed topographies (Section "Streambed-Induced (Hyporheic) Flow") to be used in the Monte Carlo sensitivity analysis of the hyporheic flow. This method provides a broad range of possible bedform variations within the catchment. Furthermore, the uncertainty in the quantitative analysis of the streambed-induced flow field was accounted for by conducting a Monte Carlo analysis based on 400 randomized combinations of hydrostatic damping factors (from a uniform distribution of [0-1]) with streambed topographies (from 20 rescaled streambed bedform variations). Finally, these 400 samples obtained from the Monte Carlo analysis were used to calculate the hydraulic head for each of the 30 clusters of deep groundwater discharge points (reflecting 30 different stream flow velocities and water depths), and the results were used to represent the uncertainty for a given cluster. Consequently, when analyzing the entire watershed, 12,000 ($=400 \times 30$) realizations of hydraulic head variability at the streambed scale were used. A summary of the samples applied in the analysis is presented in Table 1.

Particle Tracing

Particle tracking was used to identify streamlines that follow hyporheic, intermediate and deep groundwater flows. Deep groundwater was defined as flow that entered the bedrock, and intermediate groundwater was determined to only be present in Quaternary deposits. Hyporheic flow contains streamlines starting and ending in the stream bottom within a 5-m spatial scale. Particle tracking was conducted at two different spatial scales: the regional scale (i.e., entire catchment) and local scale (i.e., 5 m × 5 m × 5 m).

Regional-scale particle tracking was conducted to evaluate deep groundwater discharge zones and to distinguish the deep and intermediate groundwater flow fields (Section "Particle Tracing in Regional Groundwater Flow Fields"). In addition, particle tracking was conducted on a large number of 5 m × 5 m × 5 m containing a hyporheic

Table 1
Schematic Description and Summary of the Considered Samples in the Analysis

	Streambed-Induced Hydraulic Head Components			
	Dynamic Head Coefficient $\left(\frac{h_m}{\sigma_{S,B}\sqrt{2}}\right)$			**Hydrostatic Head Damping Factor** C_{damp}
Component				
Principal parameter	v_f	D_w	$\sigma_{S,B}$	
Description of the considered samples	30 different subcatchments (Figure S2, Supporting Information)		20 different streambed topographic variations (Figure 1b)	Random number within the 0-1 interval
Included in Monte Carlo simulation	—		✓	✓
Number of samples	30			400
Number of 5 m × 5 m × 5 m streambed-scale realizations		$30 \times 400 = 12,000$		

flow field in deep groundwater discharge zones in the absence and presence of upwelling groundwater (both deep and intermediate flows) to investigate the impact of hyporheic flow on deep groundwater discharge.

Particle Tracing in Regional Groundwater Flow Fields

A particle-tracing routine was implemented in the catchment-scale model to analyze the distribution of deep groundwater flow paths (Genel et al. 2013). A total of 10,000 inert particles was released from 100×100 uniformly spaced grid points over a flat horizontal surface located at a depth of approximately 500 m below the minimum topographic elevation and tracked over time until all the particles either exit the flow domain via the lateral sides or reach the top surface of the model. The concept of a time period in steady-state particle tracing is strictly numerical; particle tracing uses the evaluated velocity fields from the steady-state Darcy's law to determine particle positions. In this study, the flow paths of particles that reached the surface from a depth of 500 m were considered to represent the deep groundwater flow in all subsequent analyses.

Particle Tracing in Superimposed Flow Fields

The 12,000 realizations of streambed-induced flow involved 400 streambed-scale models for each of the 30 subcatchments (i.e., flow properties). Cubes of $5 \, m \times 5 \, m \times 5 \, m$ at the deep groundwater discharge zones contained groundwater flow from different spatial scales (i.e., from shallow to deep groundwater flows). In addition to deep groundwater flow, "intermediate groundwater flow" was defined from particle trajectories starting in recharge areas of the catchment flow model but confined to Quaternary deposits and sediment units (i.e., without entering the bedrock unit) (Figure 2).

The velocity vector for each cube containing intermediate and deep groundwater particles that reached the topographic surface within the catchment boundary was extracted with a resolution of 0.1 m from the catchment-scale model. The catchment-scale groundwater velocity field was superimposed on the corresponding streambed-scale velocity field, which was evaluated using the local stream flow properties at deep groundwater discharge clusters (Section "Spatial Representativity of the Streambed-Induced Flow"). Subsequently, a set of 50×50 particles with a uniform grid distance interval of 0.1 m was released at the bottom of the domain of each superimposed flow field (i.e., at a depth of 5 m). The released particles were tracked as they migrated toward their final destinations at the domain boundaries to evaluate the impact of the streambed-induced flow field on intermediate and deep groundwater flows (Figure 2). The travel times of the individual released particles in the superimposed model were evaluated.

Fragmentation of the Hyporheic Flow and Groundwater Discharge Zone

In addition to the deep groundwater travel time in the superimposed models, the analyses also covered how the

hyporheic flows affected the spatial distribution of various sizes of catchment-scale groundwater upwelling zones at streambed interfaces. The fragmentation of hyporheic, as well as groundwater, upwelling is defined as a shift in the distribution of coherent areas of upwelling hyporheic and groundwater flows at the streambed interface toward smaller areas. A coherent upwelling area is defined as a set of all adjacent areas in the numerical model with upward flow. These areas represent streambed areas with upwelling deep groundwater, whereas other areas are not subjected to upwelling deep groundwater.

The fragmentation analysis was conducted on hyporeic flow and deep groundwater flow discharge zones using the particle-tracing results for the $5 \, m \times 5 \, m \times 5 \, m$ domains with and without superimposed catchment scale and hyporheic flows. In addition, fragmentation analysis was conducted on the catchment-scale model's top surface (with a resolution of $5 \, m \times 5 \, m$) to determine the size distribution of coherent groundwater upwelling zones. Numerically, coherent upwelling areas were evaluated at the top surfaces of the streambed-scale and catchment-scale models using an orthogonal mesh with resolutions of $0.1 \, m \times 0.1 \, m$ and $5 \, m \times 5 \, m$, respectively, wherein the flow velocity values were considered only in the orthogonal directions.

Results

Groundwater Flow Field

The catchment-scale groundwater results showed that the groundwater fluxes at depths shallower than approximately 70 m were substantially influenced by the resolution of the water table DEM. The mean value of the absolute vertical velocity of the catchment-scale groundwater flow in recharge zones, $\langle |W_C| \rangle$, was used to evaluate the impact of the DEM resolution on the groundwater flow intensity. The results showed that decreasing DEM resolution (i.e., larger mesh size) only across groundwater recharge zones significantly affected $\langle |W_C| \rangle$ at the water table ($z = 0$) (Table 2 and Figure 3). In addition, the mean value of deep groundwater vertical velocity at the topographic surface slightly decreased when a larger mesh size in the DEM files was used.
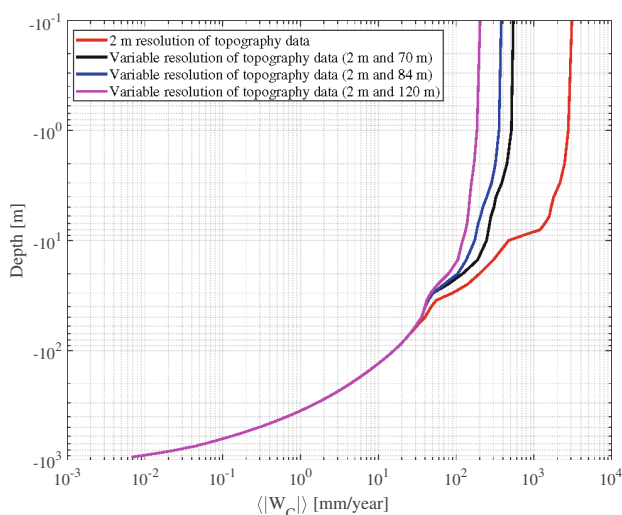
By successively revising the resolution of the topographic data in downwelling areas, we found that an 84 m resolution corresponded to $\langle |W_C| \rangle = 379$ mm/year. Since this value corresponded to the approximate estimated infiltration by the SMHI, (i.e., 382 mm/year) of this area, it was kept as a plausible model setup reflecting the intensity of groundwater circulation and, hence, the magnitudes of the discharge velocities. The results highlighted the fact that the applied resolutions of the topographic data influenced the vertical flux to a depth of 70 m but did not significantly influence the flux below this depth (Figure 3).

The discharge points of the particles released at 500-m depths were evaluated through a particle-tracing method in the catchment-scale model. The particle statistics show that 4434 ($=2743 + 1691$) of the released

NGWA.org

B.B. Mojarrad et al. Groundwater 61, no. 1: 66–85   73

Table 2
The Impact of DEM Resolution in Groundwater Recharge Zones on $\langle |W_C| \rangle$ at the Water Table ($z = 0$)

DEM Resolution in Recharge Zones (m)	DEM Resolution in Discharge Zones (m)	$\langle |W_C| \rangle$ at Water Table ($z = 0$) (mm/year)	Mean Value Of Vertical Velocity of Deep Groundwater Discharge Flow (m/s)
2	2	3073	9.91E−08
70	2	542	2.58E−08
84	2	379	1.95E−08
120	2	203	9.37E−09

Figure 3. Mean values of the absolute vertical velocity of the catchment-scale model in groundwater recharge zones, $\langle |W_C| \rangle$, as a function of depth. The results were derived using a general DEM resolution of 2 m in the discharge areas and different resolutions for the recharge areas: 2 m DEM (red line), 70 m (black line), 84 m (blue line), and 120 m (magenta line).

particles had initial positive (upward) vertical velocities, and 2743 particles reached the top surface of the model. A schematic sketch showing the details of the particle-tracing statistics is presented in Figure S3 in the supporting information. In addition, 1552 discharge points at the topographic surface were located within the catchment area, while the rest of the particles reached the top surface (i.e., 1191 particles) outside of the catchment boundaries (Figure 4). The discharge locations for the deep groundwater particles with initial positive vertical velocities at a depth of 500 m revealed that the majority of the particles reached the surface in lowland areas along the stream network and in lakes. Eleven lakes exist in the Krycklan catchment, and the results indicated that 162 particles (or 10%) representing deep groundwater discharge points reached the lakebed surface.

The catchment-scale modeling results indicated that the travel times of the inert particles (quantified using the seepage velocity) that reached the top surface of the model substantially differed among different units (i.e., bedrock, Quaternary deposit, and sediment units) (Figure 5). These results were due not only to the different porosities, hydraulic conductivities and depths of these units but also to a successive acceleration of the flow toward the top surface associated with the hierarchical structure of groundwater flow cells (Cardenas 2007; Wang et al. 2016). The results indicated that the travel times for particles released at a 500-m depth were longest in the bedrock unit (in the range of 100 to 40,000 years), while the particle travel times corresponding to the Quaternary deposit unit were substantially shorter (in the range of 2 to 120 years). The travel times of particles within the upper 5-m sediment unit were even shorter than those in the other units and varied between 0.4 and 80 years. The median travel times of the particles in the bedrock, QD, and sediment unit were approximately 750, 10, and 8 years, respectively. The inclusion of solute retardation in the subsurface strata substantially increased the travel time, especially in the Quaternary deposit and sediment units. In particular, the median transport times of ^{135}Cs in the different units were all found to be on the order of 10^3 years (i.e., the bedrock, Quaternary deposit, and sediment units).

Streambed–Induced (Hyporheic) Flow Field

The streambed-scale flow fields were quantified for 12,000 realizations (i.e., 30 subcatchments representing the local stream flow velocities and depths and 400 samples obtained by a Monte Carlo simulation with random combinations of streambed topographic variations and hydrostatic damping factors). The results demonstrated that the mean value of the absolute vertical velocity at the streambed interface, $\langle |W_S| \rangle$, always had a median value in a range of 3×10^{-6} to 9×10^{-6} (m/s) (Figure S4 in the supporting information). The dynamic coefficient varied with variations in the topographic elevation, as well as variations in the stream flow characteristics within the catchment. The contributions of the hydrostatic head and dynamic head to the total streambed hydraulic head were evaluated by comparing the results obtained through the consideration of only the hydrostatic head damping factor (Figure 6b) or dynamic head coefficient (Figure 6a and Table S2 in the supporting information).

The results showed that the Froude number ($\text{Fr} = \frac{v_f}{\sqrt{g D_w}}$) plays a major role in the relative contribution of the dynamic head coefficient; the higher the Froude number is, the larger the dynamic head contribution (Figure 6a). The reason for this is that the amplitude of
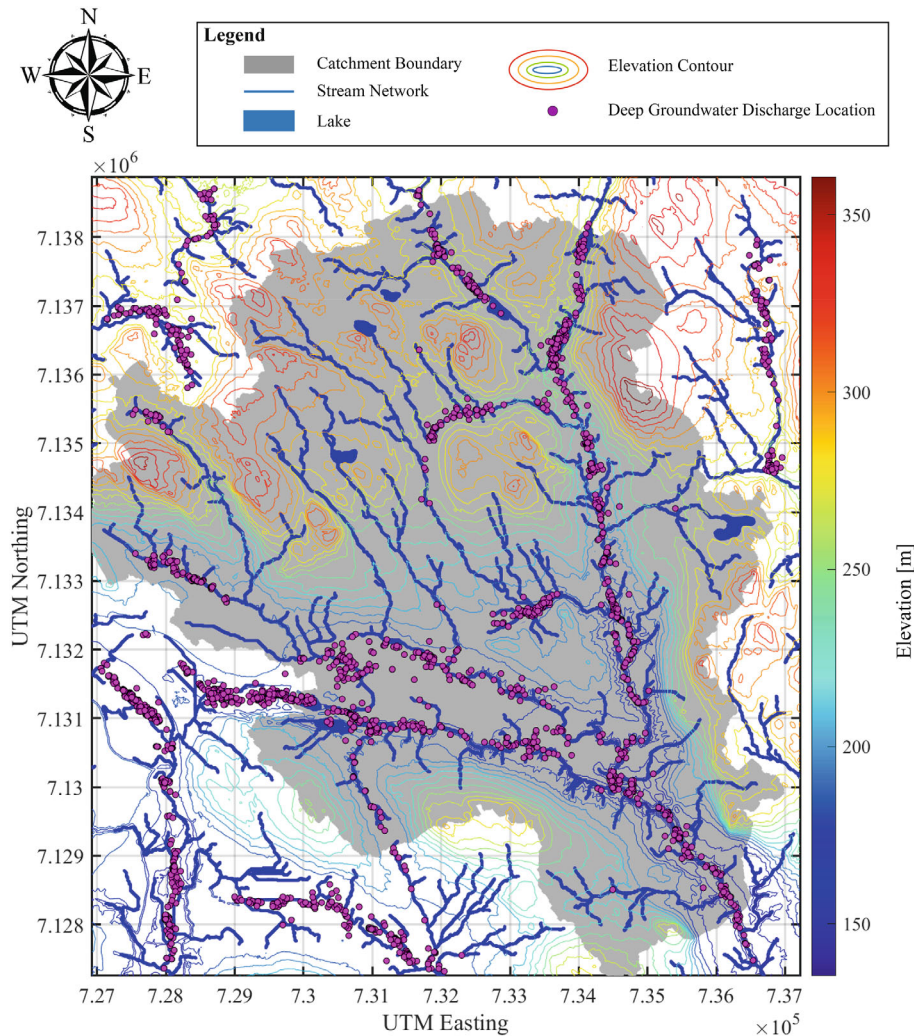
Figure 4. Discharge locations of particles released from a depth of 500 m from the minimum topographic elevation of the catchment. The discharge locations are represented by purple points. In addition, the topographic elevation range is presented with contours in which the colors range from blue to red as the elevation increases. The stream network and catchment boundary are represented by the blue line and gray zone, respectively.

the hyporheic dynamic head depends on the ratio of the squared stream flow velocity to its depth (Equation 6). The exact ratio varies with the relative penetration of bedforms (Z_{BM}/D_w), but generally, increasing the flow velocity and/or decreasing the flow depth leads to an increased contribution of the dynamic head component to the total hyporheic head. The results of the Monte Carlo simulation for the study domain revealed that the contribution of the dynamic head component became higher than that of the hydrostatic head component when the Froude number was greater than approximately 0.450. However, most samples in the applied Monte Carlo simulation had Froude numbers that were lower or even much lower than 0.45, at which the hydrostatic head component dominated the total streambed-scale hydraulic head (Figure 6c).

The Impact of Streambed–Induced Flow on the Discharge of Regional Groundwater

Three metrics were selected to assess the impacts of streambed-induced fluxes on the groundwater flow field:

(1) the travel time of groundwater flow in the streambed sediments, (2) the groundwater flow direction near the bed surface, and (3) the fragmentation of coherent groundwater upwelling areas at the sediment bed. The results revealed that the travel time of the discharging groundwater near the topographic bed surface substantially depends on the penetration depth of the groundwater flowpath. The analysis of the groundwater flow field (in the absence of a streambed-induced flow field) showed that intermediate flow paths that circulated only in Quaternary deposits had shorter travel times within the sediment unit than those of deep groundwater flow emanating from a 500-m depth (Figure 7, solid lines). In particular, the mean travel time of the intermediate groundwater flow was only approximately 1/3 of the travel time of the deep groundwater flow within the sediment unit. In addition, the superimposed flow field revealed that the streambed-induced hyporheic flow substantially decreased the travel time of the discharging groundwater within the sediment unit (Figure 7, dashed lines). This hyporheic-induced amplification of the
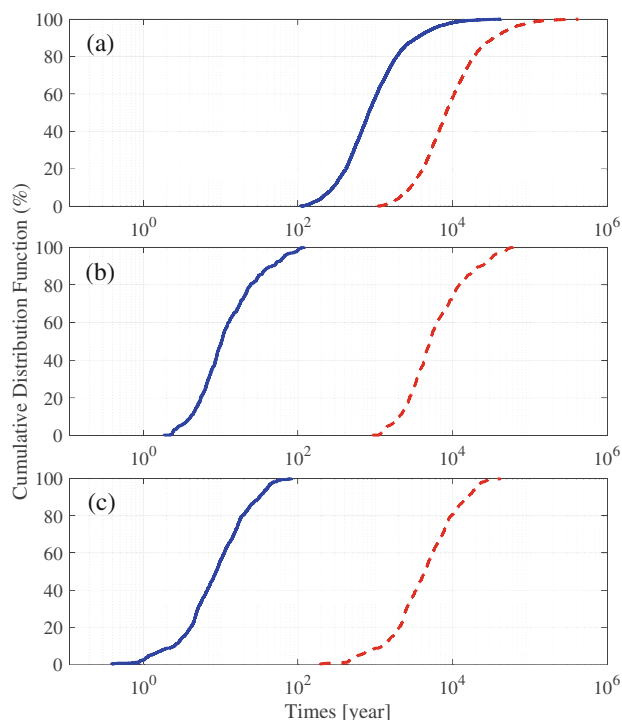
Figure 5. Cumulative distribution function plots of the water travel time (solid blue line) and ^{135}Cs transport time (dashed red line) in the (a) bedrock, (b) Quaternary deposit, and (c) sediment domains. It should be noted that the results correspond to particles with initial positive vertical velocities that were released from a depth of 500 m from the minimum topographic elevation and reached the top surface.

groundwater seepage velocity was stronger for flow paths with lower seepage velocities, that is, longer travel times, highlighting the strong influence of the streambed-induced fluxes on deep groundwater flow.

The groundwater flow directions near the streambed surface were substantially influenced by the streambed-induced fluxes and hyporheic flow. Figure 8 shows the divergence of the upward groundwater flow fields from their trajectory paths due to the presence of hyporheic flow fields in two arbitrary superimposed flow fields representing a dynamic head coefficient of 0.08 and hydrostatic damping factor, C_{damp} ($\lambda_i = 5$ m), values of 0.73 (Figure 8a and 8b) and 0.13 (Figure 8c and 8d). The depth-decaying hydraulic conductivity in the streambed-scale models controls the depth at which streambed-induced flows start to impact the groundwater flow field. Figure 8a and 8b shows that the influence of hyporheic flows on groundwater discharge begins at depths between 2.5 and 3.5 m from the topographic surface, while the impact occurs at shallower depths in Figure 8c and 8d. Due to the impact of the streambed-induced flow field, the vertical upwelling of the groundwater was found to be separated (or fragmented) into a few detached small areas of groundwater discharge at the streambed interface. A decrease in the hydrostatic damping factor (increased damping) resulted in a stronger impact of the streambed-induced flow field on the upward groundwater flow (compare Figure 8a and 8c) and resulted in smaller

upwelling areas at the streambed interface (compare Figure 8b and 8d).

The distribution of the catchment-scale groundwater upwelling areas at the streambed interface was significantly affected by the streambed-induced fluxes. To assess the fragmentation of groundwater flow at the streambed interface, the distribution of coherent upwelling areas was quantified at the top surfaces of the streambed-scale model and catchment-scale model (i.e., without consideration of hyporheic flows) with resolutions of 0.1 and 5 m, respectively. The fragmentation of the upwelling areas presented as a shift of the cumulative distribution functions, CDFs; a higher fragmentation shifted the corresponding CDF plot toward smaller areas. The fragmentation results showed that in the absence of hyporheic flow fields, 96% of the coherent upwelling areas of the regional groundwater flow were larger than the size of the streambed-scale model's top surface (i.e., discharge areas were larger than 25 m^2) (Figure 9a, solid blue line) and that the median value at the top surface was 400 m^2 (Figure 9b, dashed blue line). The deep groundwater upwelling flow accelerated and thus contracted toward the topographic surface, showing a variation in the upwelling flux area that occurred along the deep groundwater flow trajectories toward the topographic surface. In particular, the ratio of the deep groundwater upwelling area at the release point ($Area_{(z=-500\ m)}$) to the deep groundwater upwelling area at the bottom of the sediment unit ($Area_{(z=-5\ m)}$) indicated the contraction of the flow area ranging between 1×10^{-4} and 1×10^{-2} (Figure S5 in the supporting information).

On the other hand, when considering only the streambed-scale model that contained only hyporheic flow paths, the areas with coherent upwelling were found to be less than 7.5 m^2 (30% of the total streambed area) (solid red line in Figure 9). As expected, the upwelling of the streambed-induced flow was more fragmented than the upwelling of the regional groundwater flow (shifting toward smaller areas in the CDF plots). When taking the streambed-induced fluxes into account, the coherent areas of upwelling groundwater were substantially lower, with approximately 95% of coherent upwelling areas in the superimposed models being less than 1.25 m^2 (5% of the top surface of the streambed-scale model) (Figure 9, solid magenta line). Thus, by comparing the fragmentation of groundwater upwelling areas with and without streambed-induced fluxes, a strong influence of hyporheic flows on the fragmentation of groundwater upwelling areas was revealed.

Discussion

Generally, ambient groundwater affects the hyporheic depth, while the streambed-induced flow changes the upwelling groundwater in terms of both the flow velocity and flow direction near the bed surface (Cardenas and Wilson 2006; Boano et al. 2009; Mojarrad et al. 2019a). The implication is that the exchange of natural solute elements and heat emanating from deeper groundwater are affected by the presence of hyporheic flows; this is
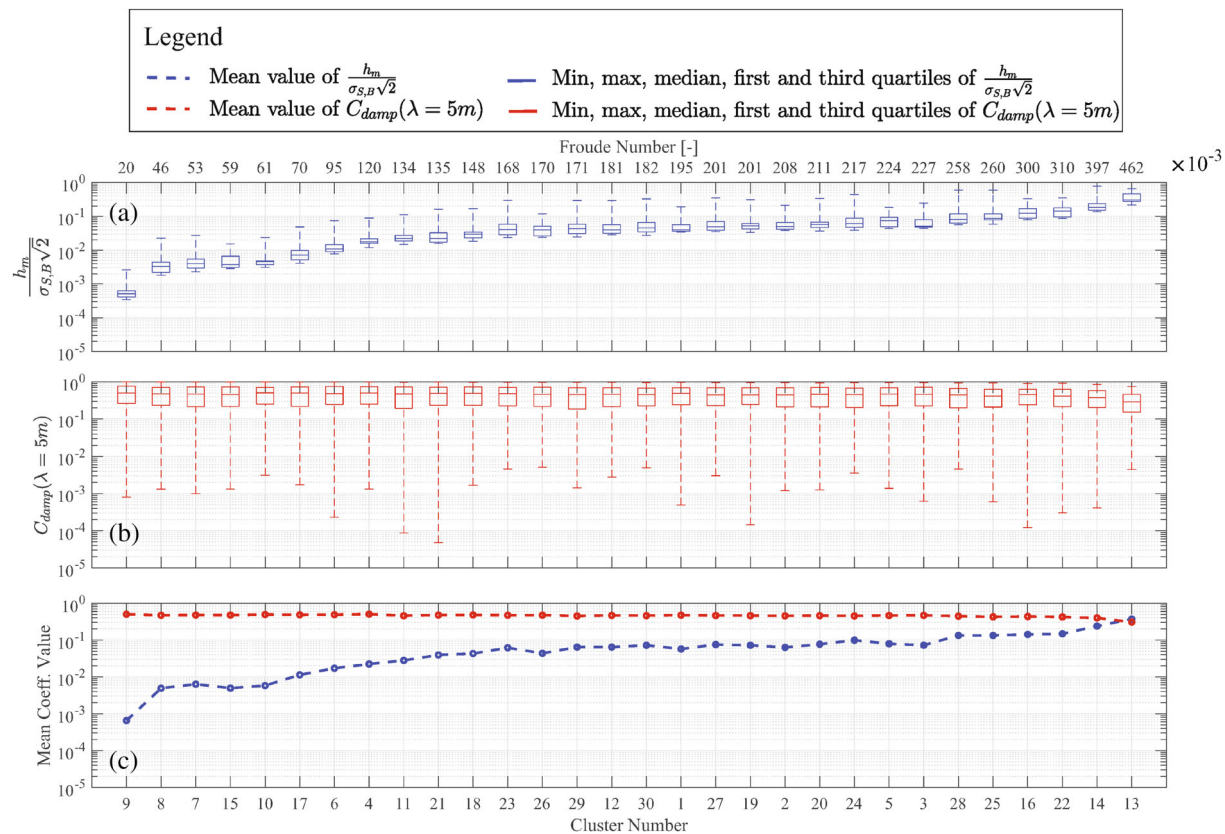
Figure 6. Streambed-induced hydraulic head factors that were used in the Monte Carlo simulation for different areas in different parts of the study catchment (Figure S2 in the supporting information for the drainage area labels) sorted by the Froude number values of the flow properties in various subcatchments: (a) the distribution of the dynamic factor for each drainage area, (b) the distribution of the hydrostatic damping factor for each drainage area, and (c) the mean dynamic coefficient (blue color) and hydrostatic damping factor (red color) values for each drainage area.

especially manifested in terms of very narrow pinholes of deep groundwater flows into surface water systems.
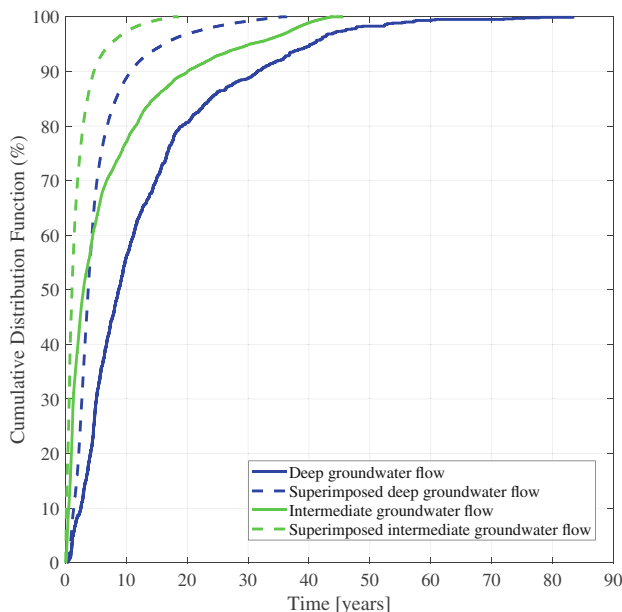
Regional Groundwater Flow Travel Time

The results of the catchment-scale modeling showed that the resolution of the topography of the groundwater table controls the modeled groundwater fluxes, similar to what has previously been found (Marklund and Wörman 2011). The natural boundary condition consists of both topography-controlled head (at lakes and streams) and recharge-controlled head (at topographic surfaces with downward flow directions) boundary conditions. The results highlighted the role of the DEM resolution in infiltration zones, which allowed us to formally apply a head boundary condition that also satisfies the natural infiltration condition. Only decreasing the DEM resolution over the recharge zones while maintaining the high DEM resolution (i.e., 2 m × 2 m) in discharge zones (i.e., stream networks, lakes, etc.), allows us to evaluate in- and exfiltration zones via discontinuities in topographic gradients throughout the river network in the catchment-scale model (Stanford and Ward 1993). Decreasing the DEM resolution over the recharge areas by itself is a simplification that can be used when the spatially distributed data of the infiltration rate are not available. Representing the groundwater table in recharge areas via

finer resolution of the DEM addresses the constraints of infiltration on the water table geometry and can be matched to the observed mean annual infiltration rate of the region.

In this study, the topography-controlled boundary condition was taken as the landscape topography at the discharge location in a stationary model. However, due to the rapid adaptability of groundwater flow to variations in boundary conditions, nonstationary conditions are less important to instantaneous groundwater discharge in the case of groundwater flow with a travel time in the range of hundreds to thousands of years. In addition, the role of hydrological variation and, in particular, the variable recharge rate, which could potentially affect the contribution of water from various spatial scales in subsurface discharge regions, was not investigated and is recognized as a limitation, especially for groundwater flows with short travel times (Dams et al. 2012).

In this study, the groundwater discharge zones were found to align well with the river network (representing 90% discharge points) and/or lakes (representing 10% discharge points), which were topographically low points in the landscape with frequent relatively deep Quaternary deposits similar to those found by Marklund et al. (2008) and Caruso et al. (2016). Previous studies have indicated that the deep groundwater discharge location at the

Figure 7. Cumulative distribution function plot of the intermediate (green color) and deep (blue color) travel times (using seepage velocity) of the groundwater flow within the sediment layer (i.e., 5 m × 5 m × 5 m); the solid lines represent the catchment-scale results (without the streambed-induced flow influence), whereas the dashed line represents the superimposed results (catchment-scale flow superimposed with the streambed-scale induced flux). Descriptions of the different flow types are presented in Figure 2.

topographic surface is primarily controlled by topographic variation, and the distribution of the fracture network only slightly affects the discharge locations (Selroos et al. 2002; Marklund et al. 2008; Welch et al. 2012). In the absence of detailed data for the study region, the bedrock was assumed to be a continuum subsurface stratum with average hydraulic conductivity, and the horizontally constant hydraulic conductivity was assumed to decay with depth (Figure 2). Depth-decaying hydraulic conductivity has previously been suggested for the Krycklan catchment (e.g., Ameli et al. 2016b). Moreover, in the present study, the applied depth-decaying hydraulic conductivity function was based on regional hydraulic conductivity field measurements conducted by Swedish Nuclear Fuel and Waste Management, SKB (Ericsson et al. 2006). Horizontal variability in the hydraulic conductivity was assumed, but only for the overlying soil strata (Quaternary deposits and possible aquatic sediments). These uppermost units have a dominant effect on the discharge of groundwater, and thus, we believe that this simplified model represents the most important patterns in hydraulic conductivity.

In addition, the locations of discharge zones at the topographic surface adapt relatively quickly to changes in boundary conditions, and the location of discharge follows the valleys in the lowlands, which could vary slightly within less than 3 mega-annum (mega-annum abbreviated as Ma, where 1 Ma is equal to 1 million years) in northern Sweden (Lidmar-Bergström 1996). Since our results for

groundwater transport time (Figure 5) are in the range of hundreds to thousands of years, they are representative of stationary/quasi-stationary conditions but not necessarily of a specific historic or future period transport scenario.

The particle tracing results of this study showed that the travel times of groundwater flows in bedrock with thicknesses greater than 450 m were in the range of 100 to 40,000 years, which confirms the findings of Ericsson et al. (2006). However, the median value of the groundwater travel time in the bedrock unit in our study slightly differs from what Ericsson et al. (2006) found (750 and 1200 years, respectively). The difference between the median groundwater travel time in the bedrock unit determined in this study and that determined by Ericsson et al. (2006) is due to the variation in the study areas, which is reflected, for example, in the thicknesses of the bedrock units, as well as in the differences in the applied function describing how the hydraulic conductivity decays with depth. Each particle in the applied particle tracing represents a fraction of release plane area. While the represented upward flow by each particle is constant; the flow area decreases toward the topography surface due to impacts from the nested multiscale flow fields (Figure S5 in the supporting information). Hence, the flow velocity increases according to the flow continuity reason (i.e., flow velocity and flow area are correlated inversely).

The travel times of the catchment-scale groundwater vary among different units due to variations in the unit thickness, porosity, and hydraulic conductivity values. Furthermore, the solute transport time is longer than the water travel time due to the retardation induced by sorption and diffusion processes. Solute and contaminant retardation varies between different subsurface strata and depends on several parameters, such as soil porosity, the fracture size of the bedrock, and the ratio of adsorbed mass to dissolved mass within the subsurface unit (Kutílek and Nielsen 1994; Xu and Wörman 1999; Wörman et al. 2004). Hence, a higher retardation factor in Quaternary deposits and sediments compared with that in bedrock leads to the accumulation of solutes and contaminants within aquatic sediment for long periods of time, which needs to be considered in solute and contaminant fate and transport. The retardation coefficient is usually considered a constant value for a given material, but the spatial heterogeneity in the permeability of a single subsurface unit (e.g., sediment) leads to heterogeneous retardation coefficients (Piqué et al. 2013). In addition, the retardation coefficient is determined using breakthrough curves, BTCs (Li et al. 2009), in which increased groundwater flow velocities near the bed surface that occur due to the impact of the hyporheic flow fields change the shapes of the BTCs and, consequently, the values of the retardation coefficients of streambed sediments.

Nested groundwater flow systems comprise subsurface flows across a wide range of spatial scales, all with different flow properties. The applied multiscale approach of this study addresses regional, intermediate
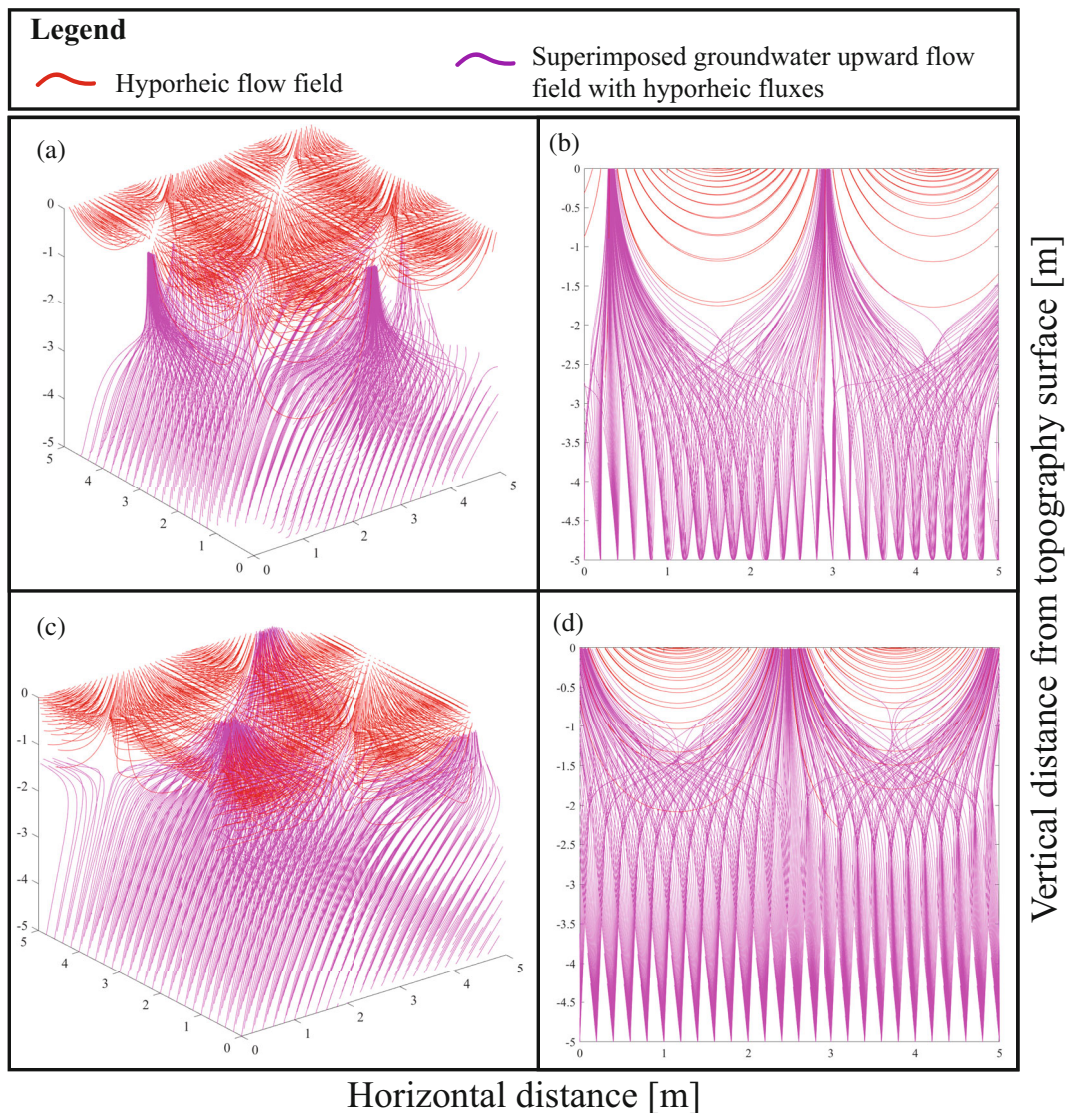
Figure 8. The impact of hyporheic fluxes (red lines) on the upwards groundwater flow (magenta lines) in the superimposed models (including both intermediate and deep groundwater flows). The figure corresponds to 2 arbitrary superimposed cases using a dynamic head coefficient of 0.08, hydrostatic damping factor of 0.73 (a and b) and a hydrostatic damping factor of 0.13 (c and d); (a) and (c) display three-dimensional views; and (b) and (d) display side views.

and hyporheic flow systems, which is consistent with the hierarchically nested groundwater flow cells first described by Tóth (1963). In addition to basin geometry and the surface topography, as described by Tóth (1963), the geological heterogeneity of the subsurface hydraulic conductivity, such as dependent on stratification and soil type, significantly impacts the local, intermediate and regional groundwater flow velocity and discharge zones (Freeze and Witherspoon 1967; Jiang et al. 2010, 2011). In particular, the soil heterogeneity can potentially enhance or hinder the groundwater flow; hence, the location and size of groundwater discharge zones often follow the geological heterogeneity (Cardenas and Wilson 2007; Sawyer and Cardenas 2009). Fracture zones could also emphasize or counteract groundwater flow circulation, but it does not significantly alter the behavior of mean groundwater flow (Gelhar and Axness 1983). In this study, deep

groundwater flows mostly reached the topographic surface downstream in the lowest part of the catchment, which also had a lower slope and contained soils with higher hydraulic conductivity than the upper part of the catchment (e.g., Figure 4).

Furthermore, this study also separates the treatment of discharge and recharge zones by applying different top boundary conditions, and the local-scale investigation focuses on the boundary conditions that arise in surface water systems and impact hyporheic flow. These interactions have not been considered in the previous literature incorporating the subsurface flow-nested perspective. In this study, the modeled water travel times for the intermediate groundwater flowing from recharge areas to discharge points throughout the entire catchment are presented in Figure 7. The median value is approximately 2.5 years, which is on the same order of magnitude as the

A (m²): Coherent Upwelling Areas at the Streambed Interface
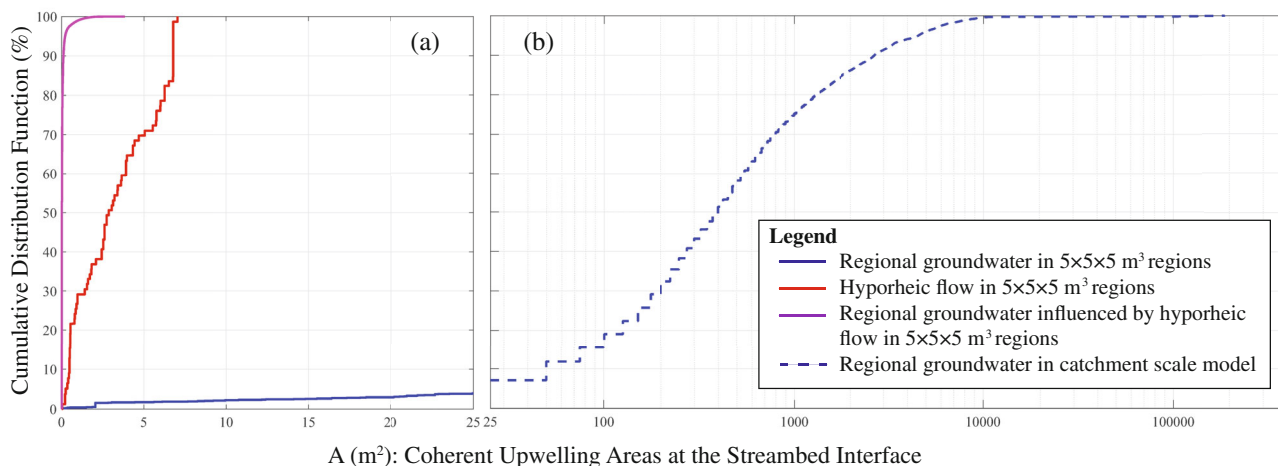
Figure 9. Cumulative distribution function plot of the coherent upwelling areas at the streambed interface for (a) groundwater flows (i.e., solid blue line), hyporheic exchange flows (i.e., solid red line), and groundwater flows influenced by hyporheic exchange fluxes (i.e., solid magenta line) in 5 m × 5 m × 5 m regions and (b) groundwater flows (dashed blue line) in the catchment-scale model.

results (1.2 to 7.7 years) obtained by a recently published study performed in the same catchment area (Jutebring Sterte et al. 2021). The results showed a substantial difference in the sizes of the discharge areas of the regional groundwater and hyporheic flows at the streambed interface (Figure 9), in which the groundwater flow discharge area was significantly fragmented into smaller areas under the influence of hyporheic fluxes. Hence, in addition to the previously determined characteristics, such as groundwater trajectories (Vissers and van der Perk 2008; Wang et al. 2014) and the groundwater residence time distribution (Wang et al. 2016), the sizes of the discharge areas of subsurface flows at the streambed interface can be used to distinguish the regional and hyporheic flows in hierarchically nested groundwater flow systems. The investigation of hierarchically nested groundwater flow systems improves our understanding of quantitative and qualitative groundwater flow-related phenomena, including the fate and transport of solutes and contaminants (Zijl 1999).

Representativity of the Streambed–Induced Flow Field

The streambed-induced flow field depends on the contributions of the hydrostatic and dynamic hydraulic heads to the head boundary condition at the streambed-subsurface interface. The stream Froude number and streambed topographic variation are primary factors that control the hydrostatic and dynamic contributions to the pressure along the streambed (Tonina and Buffington 2007; Käser et al. 2013). The stream bedform variations governing hyporheic flows were represented by selecting 100 m × 100 m representative areas from the entire catchment, which were then rescaled to streambed topography and used in Monte Carlo simulations. Therefore, the result of this study stands for the hyporheic and superimposed flow fields that are in the range of considered bedform variations in Table S3 of supporting information.

The rescaling of streambeds applied in this paper is consistent with the known fractal distributions between streambed and continental landscape scales (Hino 1968; Nikora et al. 1997; Turcotte 1997; Wörman et al. 2007a, 2007b); however, it also assumes a similarity in the actual (real) shape, which we assume is only a regional behavioral trait. Although this procedure is not supported by previous studies, it provides an estimate of streambed topography when such data are lacking over larger regions. This approach implies that the spatially average flux follows the power spectral density of the topography (Morén et al. 2017, Equation (7a)), but it is only used to qualitatively demonstrate the nature of the hyporheic flow fields. Mojarrad et al. (2019b) demonstrated that the uncertainty in the hydrostatic damping factor has a substantial impact on the streambed-induced flow field. Field experiments reported in the literature indicate that there is high uncertainty in the hydrostatic damping factor at spatial scales less than 20 m (Morén et al. 2017; Mojarrad et al. 2019b).

In this study, a Monte Carlo simulation with 400 randomized combinations of hydrostatic damping factors (from a uniform distribution ranging between 0 and 1) and streambed topographies (from 20 different realizations) was used in a sensitivity analysis of hyporheic flows. In addition, the streambed-induced dynamic head was evaluated using data from the available discharge stations and the corresponding drainage area of each of 30 subcatchments (i.e., discharge clusters), along with the mean values of the physical characteristics of the stream segments. Thus, the statistical (aleatoric) uncertainty in the hydrostatic and dynamic head contributions to the total hyporheic hydraulic head was addressed using the applied Monte Carlo sampling approach.

The hydrostatic head component dominated most of the streambed-scale total hydraulic head is consistent with the previous findings of Mojarrad et al. (2019b). The depth-decaying hydraulic conductivity behavior of

streambed sediment has been demonstrated in previous research using field-measured data (Ryan and Boufadel 2007; Song et al. 2007). These studies generally confirmed the presence of depth decay in the hydraulic conductivity, which is more pronounced at shallow depths and then decreases with depth similarly to an exponential function (Singh et al. 2014). Therefore, in this study, we recognized the depth-decaying trend in hydraulic conductivity, and the exponential decay function was fitted to the general stream data measured by Morén et al. (2017). Furthermore, one can consider how grain-size distributions and soil porosity vary with depth and theoretically argue that these trends would affect the hydraulic conductivity that supports the selection of the functional type. As a consequence, the epistemic (systematic) uncertainty included in the hyporheic flow fields, which is induced by the depth-decaying hydraulic conductivity function and the spatial heterogeneity of streambed sediments, was not recognized in this study.

Dominant Behavior of the Streambed–Induced Fluxes

In hierarchically structured groundwater flows, upwelling groundwater is known to converge and accelerate toward discharge zones (Wang et al. 2016), but in addition, our findings emphasize that this convergence phenomenon is particularly strong near streambeds due to the impact of hyporheic fluxes (Figure 8). As a consequence, the distribution of the coherent groundwater upwelling areas was found to be shifted toward much smaller regions that resembled pinholes at the streambed where the deep groundwater flow penetrated through hyporheic flow (Figures 8 and 9). This effect can be seen as a "fragmentation" of the discharge zones. The results of the pinhole groundwater discharge pattern found in this study confirm the findings of Lidman et al. (2013), who observed small areas of groundwater discharge through a field investigation using uranium, thorium, and radium measurements, and findings by and Ploum et al. (2018), who used a variety of data, including temperature signals from groundwater in surface water.

Since the distribution of flow paths in the sediments is highly important for understanding the hydrological, biological and ecological processes at the streambed interface (Mathers et al. 2014; Mendoza-Lera and Datry 2017; Fox et al. 2018), the revealed convergence of groundwater flow paths near the streambed interface is hypothesized to be of great importance for groundwater-surface water exchange processes. The temperature differences between deep groundwater flows and hyporheic exchange fluxes (Mamer and Lowry 2013) reflect a pronounced spatial focusing of the discharge zones of heat and mass transfers emanating from deep groundwater due to the strong pinhole behavior of groundwater at the streambed interface. The degree of groundwater discharge convergence and fragmentation substantially depends on the magnitudes of the streambed-induced fluxes and the vertical velocities of groundwater flows, especially their ratio. Therefore, it is clear from the model approach used in this study that fragmentation of groundwater discharge is much more

pronounced in streambed sediments than in lake bottoms that are less subjected to hyporheic flows.

The correlation between the fragmentation of discharge zones and the flow travel time was not directly investigated in this study, but the reductions in travel time of both intermediate and deep groundwater flow (Figure 7) and in the discharge areas of the groundwater flow in the streambed sediment (Figure 9) in the presence of a hyporheic flow field suggest an inverse correlation between fragmentation and the travel time of the flow. This indicates that the greater the fragmentation is, the lower the groundwater flow travel time. This finding could be expected due to flow continuity, whereby the discharge area and time are directly correlated for a constant flow tube and for approximately the same flow trajectory. Thus, as the groundwater flow converges in smaller areas due to the streambed-induced fluxes, the flow velocities increase for both the intermediate and deep groundwater. The travel time of the flow has an inverse relationship with the flow velocity, indicating that higher velocities reduce the flow travel times of aquatic sediments (Figure 7). An implication of these results is that relatively shorter groundwater flow travel times within the streambed sediment impact hyporheic habitat diversity and, consequently, stream water quality (Poole et al. 2006). A particular effect is due to the solute and contaminant fate and transport; the accumulation of solutes in stream water sediment depends on (1) the location and size of the groundwater upwelling discharge areas and (2) the deep groundwater travel times in the streambed sediments. Our results indicated that streambed-induced fluxes slightly relocate the groundwater upwelling discharge points (Figure 8). This is due to local spatial scales connected to streambed-induced flows. However, more importantly, the hyporheic flow fragments the groundwater upwelling areas and induces shorter groundwater travel times near the bed surface. An implication of results is the radionuclide fate and transport where the radionuclide rate transfer coefficient in a compartment model is inversely proportional to the groundwater travel time and upwelling discharge area (Xu et al. 2008; Wörman et al. 2019); the shorter travel time near the bed surface and smaller size of the coherent upwelling areas result in a higher transfer rate coefficient (Figure S6, supporting information).

Uncertainties in the Modeling Approach

An overarching uncertainty of the modeling approach is the relatively complicated model set up with numerous parameters, which collectively are constrained by observed magnitudes of both groundwater circulation and hyporheic fluxes in streams. For example, groundwater infiltration is constrained by observed values (Table 2 and Figure 3), and the hyporheic exchange values at discharge points in the stream network (Figure 6) are consistent with values observed using stream tracer tests (Stonedahl et al. 2010; Morén et al. 2017) and other measuring methods in the field (Bhaskar et al. 2012; Gomez-Velez et al. 2014). Moreover, hydraulic conductivity is a primary controlling factor for the spatial variability of both

hyporheic and regional groundwater flows due to its linear role in Darcy's law; thus, it causes a correlation in terms of the intensity of the two flow types. The regional groundwater flow, however, is controlled by hydraulic conductivity over larger distances, and generally, the flow intensity is dominated by lower values of hydraulic conductivity (i.e., those found in bedrock). This is because the average hydraulic conductivity over a flowpath is given by the harmonic mean weighted by the distance of the path. In addition to the hyporheic and regional groundwater flow velocities, the heterogeneity of a subsurface and, in particular, how the hydraulic conductivity decays with depth have primary controls on the distribution of hyporheic flow paths (Earon et al. 2020) and thus also strongly influence the depth where the contraction of the near-bed groundwater flow paths begins.

Conclusion

Hyporheic fluxes generally have a substantial impact on groundwater discharge in surface waters due to their much higher intensity than groundwater flows. Major conclusions of the study are the following:

- Travel times for upwelling groundwater through aquatic sediments in streams are significantly affected by the presence of the hyporheic zone. The results show that the travel times for both groundwater circulating only in Quaternary deposits and groundwater originating from deep bedrock decreased more than 50% in the upper 5 m of aquatic sediments compared to when the hyporheic fluxes were omitted.
- Close to the groundwater-streambed interface, there is a strong convergence of the groundwater discharge that appears as stream tubes forming narrow "pinholes" penetrating through the more spatially extended and intense hyporheic flow zone. This convergence phenomenon is related to previously found phenomena called discrete riparian inflow points (DRIPs) in the scientific literature and generally occurs for the investigated groundwater discharge. Groundwater discharge convergence led to a shift in the distribution of discharge areas toward smaller areas, an effect referred to herein as "fragmentation" of the groundwater discharge. Due to continuity reasons, fragmentation causes an increase in groundwater flow velocities and a spatial acceleration of groundwater discharge toward the streambed.
- The degree of convergence of the groundwater discharge is governed by the relative intensities of groundwater circulation and hyporheic flows, the spatial hydraulic conductivity of the streambed sediments and, especially, how the hydraulic conductivity decays with depth.
- Although the groundwater flow travel times from a depth of 500 m below the topographic surface are substantially different through bedrock, Quaternary deposits and aquatic sediments, the strongly adsorbing nuclide ^{135}Cs shows similar through-travel times between these units.

- The convergence of the groundwater flow and reduced groundwater travel time near the streambeds would lead to increased transfer rate coefficients using compartment models (defined by ODE systems) to represent the transport of solutes in discharge zones. Simultaneously, such models should also be adopted to the higher spatial focusing of the upwelling.
- In the deep groundwater discharge zones, the hyporheic flow is primarily controlled by the water surface elevations of the subcritical flow, that is, by the hydrostatic head component rather than the dynamic one. The relative importance of the dynamic head increases with the Froude number, which may substantially vary spatially and over time.
- Deep groundwater primarily discharges along the drainage network constituted by streams, wetlands and lakes. The strong convergence of groundwater discharge causes fragmentation in many small areas but is clustered in the lowland and downstream parts of the catchment. This clustering is primarily caused by topographic control of the regional groundwater circulation, and the discharge regions are characterized by relatively thicker Quaternary deposits.

Authors' Note

The authors do not have any conflicts of interest or financial disclosures to report.

Supporting Information

Additional supporting information may be found online in the Supporting Information section at the end of the article. Supporting Information is generally *not* peer reviewed.

Appendix S1 Supporting information

References

Ameli, A., J. McDonnell, and K. Bishop. 2016a. The exponential decline in saturated hydraulic conductivity with depth: A novel method for exploring its effect on water flow paths and transit time distribution. *Hydrological Processes* 30, no. 14: 2438–2450.

Ameli, A., N. Amvrosiadi, T. Grabs, H. Laudon, I. Creed, J. McDonnell, and K. Bishop. 2016b. Hillslope permeability architecture controls on subsurface transit time distribution and flow paths. *Journal of Hydrology* 543: 17–30.

Berglund, S., U. Kautsky, T. Lindborg, and J.O. Selroos. 2009. Integration of hydrological and ecological modelling for the assessment of a nuclear waste repository. *Hydrogeology Journal* 17, no. 1: 95–113.

Bhaskar, A.S., J.W. Harvey, and E.J. Henry. 2012. Resolving hyporheic and groundwater components of streambed water flux using heat as a tracer. *Water Resources Research* 48, no. 8: 1–16.

Boano, F., R. Revelli, and L. Ridolfi. 2009. Quantifying the impact of groundwater discharge on the surface–subsurface exchange. *Hydrological Processes: An International Journal* 23, no. 15: 2108–2116.

Boano, F., R. Revelli, and L. Ridolfi. 2008. Reduction of the hyporheic zone volume due to the stream-aquifer interaction. *Geophysical Research Letters* 35, no. 9: 1–5.

Bresciani, E., T. Gleeson, P. Goderniaux, J.R. de Dreuzy, A. Werner, A. Wörman, W. Zijl, and O. Batelaan. 2016a. Groundwater flow systems theory: Research challenges beyond the specified-head top boundary condition. *Hydrogeology Journal* 24, no. 5: 1087–1090.

Bresciani, E., P. Goderniaux, and O. Batelaan. 2016b. Hydrogeological controls of water table-land surface interactions. *Geophysical Research Letters* 43, no. 18: 9653–9661.

Cardenas, M.B. 2007. Potential contribution of topography-driven regional groundwater flow to fractal stream chemistry: Residence time distribution analysis of Tóth flow. *Geophysical Research Letters* 34, no. 5: 1–5.

Cardenas, M.B., and J. Wilson. 2007. Exchange across a sediment–water interface with ambient groundwater discharge. *Journal of Hydrology* 346, no. 3–4: 69–80.

Cardenas, M.B., and J. Wilson. 2006. The influence of ambient groundwater discharge on exchange zones induced by current–bedform interactions. *Journal of Hydrology* 331, no. 1–2: 103–109.

Caruso, A., L. Ridolfi, and F. Boano. 2016. Impact of watershed topography on hyporheic exchange. *Advances in Water Resources* 94: 400–411.

Dams, J., E. Salvadore, T.V. Daele, V. Ntegeka, P. Willems, and O. Batelaan. 2012. Spatio-temporal impact of climate change on the groundwater system. *Hydrology and Earth System Sciences* 16, no. 5: 1517–1531.

Dimova, N.T., and W.C. Burnett. 2011. Evaluation of groundwater discharge into small lakes based on the temporal distribution of radon-222. *Limnology and Oceanography* 56, no. 2: 486–494.

Earon, R., J. Riml, L. Wu, and B. Olofsson. 2020. Insight into the influence of local streambed heterogeneity on hyporheic-zone flow characteristics. *Hydrogeology Journal* 28, no. 8: 2697–2712.

Elliott, A.H., and N.H. Brooks. 1997a. Transfer of nonsorbing solutes to a streambed with bed forms: Theory. *Water Resources Research* 33, no. 1: 123–136.

Elliott, A.H., and N.H. Brooks. 1997b. Transfer of nonsorbing solutes to a streambed with bed forms: Laboratory experiments. *Water Resources Research* 33, no. 1: 137–151.

Ericsson, L.O., J. Holmen, I. Rhen, and N. Blomquist. 2006. Supra regional ground water modelling-in-depth analysis of the groundwater flow patterns in eastern Smaaland. Comparison with different conceptual descriptions; Storregional grundvattenmodellering-foerdjupad analys av floedesfoerhaallanden i oestra Smaaland. Jaemfoerelse av olika konceptuella beskrivningar. Svensk kärnbränslehantering (SKB) Techinal Report R-06-64.

Fehlman, H.M. 1985. Resistance components and velocity distributions of open channel flows over bedforms. Ph.D. diss., Department of Civil and Environmental Engineering, Colorado State University.

Fleckenstein, J.H., S. Krause, D.M. Hannah, and F. Boano. 2010. Groundwater-surface water interactions: New methods and models to improve understanding of processes and dynamics. *Advances in Water Resources* 33, no. 11: 1291–1295.

Fox, A., A.I. Packman, F. Boano, C.B. Phillips, and S. Arnon. 2018. Interactions between suspended kaolinite deposition and hyporheic exchange flux under losing and gaining flow conditions. *Geophysical Research Letters* 45, no. 9: 4077–4085.

Fox, A., G. Laube, C. Schmidt, J. Fleckenstein, and S. Arnon. 2016. The effect of losing and gaining flow conditions on hyporheic exchange in heterogeneous streambeds. *Water Resources Research* 52, no. 9: 7460–7477.

Freeze, R.A., and P. Witherspoon. 1967. Theoretical analysis of regional groundwater flow: 2. Effect of water-table configuration and subsurface permeability variation. *Water Resources Research* 3, no. 2: 623–634.

Gelhar, L.W., and C.L. Axness. 1983. Three-dimensional stochastic analysis of macrodispersion in aquifers. *Water Resources Research* 19, no. 1: 161–180.

Genel, S., M. Vogelsberger, D. Nelson, D. Sijacki, V. Springel, and L. Hernquist. 2013. Following the flow: Tracer particles in astrophysical fluid simulations. *Monthly Notices of the Royal Astronomical Society* 435, no. 2: 1426–1442.

Gomez-Velez, J.D., S. Krause, and J.L. Wilson. 2014. Effect of low-permeability layers on spatial patterns of hyporheic exchange and groundwater upwelling. *Water Resources Research* 50, no. 6: 5196–5215.

Grant, S.B., K. Stolzenbach, M. Azizian, M.J. Stewardson, F. Boano, and L. Bardini. 2014. First-order contaminant removal in the hyporheic zone of streams: Physical insights from a simple analytical model. *Environmental Science & Technology* 48, no. 19: 11369–11378.

Haitjema, H.M., and S. Mitchell-Bruker. 2005. Are water tables a subdued replica of the topography? *Groundwater* 43, no. 6: 781–786.

Hassan, M.A., D. Tonina, R.D. Beckie, and M. Kinnear. 2015. The effects of discharge and slope on hyporheic flow in step-pool morphologies. *Hydrological Processes* 29, no. 3: 419–433.

Hino, M. 1968. Equilibrium-range spectra of sand waves formed by flowing water. *Journal of Fluid Mechanics* 34, no. 3: 565–573.

Hjerpe, T., and R. Broed. 2010. Radionuclide transport and dose assessment modelling in biosphere assessment 2009. Posiva Oy Report WR-10-79.

Ingebritsen, S., and C.E. Manning. 1999. Geological implications of a permeability-depth curve for the continental crust. *Geology* 27, no. 12: 1107–1110.

Jakubick, A. 1979. Analysis of Pu-release consequences on the environmental geochemistry. In *Scientific Basis for Nuclear Waste Management*, 427–434. Boston, Massachusetts: Springer.

Jansson, R., H. Laudon, E. Johansson, and C. Augspurger. 2007. The importance of groundwater discharge for plant species number in riparian zones. *Ecology* 88, no. 1: 131–139.

Jiang, X.W., X.S. Wang, L. Wan, and S. Ge. 2011. An analytical study on stagnation points in nested flow systems in basins with depth-decaying hydraulic conductivity. *Water Resources Research* 47, no. 1: 1–16.

Jiang, X.W., L. Wan, M.B. Cardenas, S. Ge, and X.S. Wang. 2010. Simultaneous rejuvenation and aging of groundwater in basins due to depth-decaying hydraulic conductivity and porosity. *Geophysical Research Letters* 37, no. 5: 1–5.

Jiang, X.W., L. Wan, X.S. Wang, S. Ge, and J. Liu. 2009. Effect of exponential decay in hydraulic conductivity with depth on regional groundwater flow. *Geophysical Research Letters* 36, no. 24: 1–4.

Jutebring Sterte, E., F. Lidman, E. Lindborg, Y. Sjöberg, and H. Laudon. 2021. How catchment characteristics influence hydrological pathways and travel times in a boreal landscape. *Hydrology and Earth System Sciences* 25, no. 4: 2133–2158.

Käser, D., A. Binley, and A.L. Heathwaite. 2013. On the importance of considering channel microforms in groundwater models of hyporheic exchange. *River Research and Applications* 29, no. 4: 528–535.

NGWA.org

B.B. Mojarrad et al. Groundwater 61, no. 1: 66–85   83

Kautsky, U., T. Lindborg, and J. Valentin. 2013. Humans and ecosystems over the coming millennia: Overview of a biosphere assessment of radioactive waste disposal in Sweden. *Ambio* 42, no. 4: 383–392.

Kuglerová, L., R. Jansson, A. Ågren, H. Laudon, and B. Malm-Renöfält. 2014. Groundwater discharge creates hotspots of riparian plant species richness in a boreal forest stream network. *Ecology* 95, no. 3: 715–725.

Kutílek, M., and D.R. Nielsen. 1994. *Soil Hydrology: Texbook for Students of Soil Science, Agriculture, Forestry, Geoecology, Hydrology, Geomorphology and Other Related Disciplines*. Cremlingen-Destedt: Catena Verlag.

Laudon, H., I. Taberman, A. Ågren, M. Futter, M. Ottosson-Löfvenius, and K. Bishop. 2013. The Krycklan Catchment Study—A flagship infrastructure for hydrology, biogeochemistry, and climate research in the boreal landscape. *Water Resources Research* 49, no. 10: 7154–7158.

Lidman, F., A. Peralta-Tapia, A. Vesterlund, and H. Laudon. 2016. 234U/238U in a boreal stream network—Relationship to hydrological events, groundwater and scale. *Chemical Geology* 420, no. 420: 240–250.

Lidman, F., H. Ramebäck, Å. Bengtsson, and H. Laudon. 2013. Distribution and transport of radionuclides in a boreal mire-assessing past, present and future accumulation of uranium, thorium and radium. *Journal of Environmental Radioactivity* 121: 87–97.

Lidmar-Bergström, K. 1996. Long term morphotectonic evolution in Sweden. *Geomorphology* 16, no. 1: 33–59.

Li, M.H., T.H. Wang, and S.P. Teng. 2009. Experimental and numerical investigations of effect of column length on retardation factor determination: a case study of cesium transport in crushed granite. *Journal of Hazardous Materials* 162, no. 1: 530–535.

Lyon, S.W., T. Grabs, H. Laudon, K.H. Bishop, and J. Seibert. 2011. Variability of groundwater levels and total organic carbon in the riparian zone of a boreal catchment. *Journal of Geophysical Research: Biogeosciences* 116, no. G1: 1–12.

Mamer, E.A., and C.S. Lowry. 2013. Locating and quantifying spatially distributed groundwater/surface water interactions using temperature signals with paired fiber-optic cables. *Water Resources Research* 49, no. 11: 7670–7680.

Marklund, L., and A. Wörman. 2011. The use of spectral analysis-based exact solutions to characterize topography-controlled groundwater flow. *Hydrogeology Journal* 19, no. 8: 1531–1543.

Marklund, L., A. Wörman, J. Geier, E. Simic, and B. Dverstorp. 2008. Impact of landscape topography and Quaternary overburden on the performance of a geological repository of nuclear waste. *Nuclear Technology* 163, no. 1: 165–179.

Mathers, K.L., J. Millett, A.L. Robertson, R. Stubbington, and P.J. Wood. 2014. Faunal response to benthic and hyporheic sedimentation varies with direction of vertical hydrological exchange. *Freshwater Biology* 59, no. 11: 2278–2289.

Mendoza-Lera, C., and T. Datry. 2017. Relating hydraulic conductivity and hyporheic zone biogeochemical processing to conserve and restore river ecosystem services. *Science of the Total Environment* 579: 1815–1821.

Mojarrad, B.B., A. Betterle, T. Singh, C. Olid, and A. Wörman. 2019a. The effect of stream discharge on hyporheic exchange. *Water* 11, no. 7: 1436.

Mojarrad, B.B., J. Riml, A. Wörman, and H. Laudon. 2019b. Fragmentation of the hyporheic zone due to regional groundwater circulation. *Water Resources Research* 55, no. 2: 1242–1262.

Morén, I., A. Wörman, and J. Riml. 2017. Design of remediation actions for nutrient mitigation in the hyporheic zone. *Water Resources Research* 53, no. 11: 8872–8899.

Neretnieks, I. 1979. Analysis of some tracer runs in granite rock using a fissure model. In *Scientific Basis for Nuclear Waste Management*, 411–415. Boston, Massachusetts: Springer.

Nikora, V.I., A.N. Sukhodolov, and P.M. Rowinski. 1997. Statistical sand wave dynamics in one-directional water flows. *Journal of Fluid Mechanics* 351: 17–39.

Piqué, À., D. Arcos, F. Grandia, J. Molinero, L. Duro, and S. Berglund. 2013. Conceptual and numerical modeling of radionuclide transport and retention in near-surface systems. *Ambio* 42, no. 4: 476–487.

Ploum, S.W., J.A. Leach, H. Laudon, and L. Kuglerová. 2021. Groundwater, soil, and vegetation interactions at discrete riparian inflow points (DRIPs) and implications for boreal streams. *Frontiers in Water* 3: 78.

Ploum, S.W., J.A. Leach, L. Kuglerová, and H. Laudon. 2018. Thermal detection of discrete riparian inflow points (DRIPs) during contrasting hydrological events. *Hydrological Processes* 32, no. 19: 3049–3050.

Poole, G.C., J.A. Stanford, S.W. Running, and C.A. Frissell. 2006. Multiscale geomorphic drivers of groundwater flow paths: Subsurface hydrologic dynamics and hyporheic habitat diversity. *Journal of the North American Benthological Society* 25, no. 2: 288–303.

Ryan, R.J., and M.C. Boufadel. 2007. Evaluation of streambed hydraulic conductivity heterogeneity in an urban watershed. *Stochastic Environmental Research and Risk Assessment* 21, no. 4: 309–316.

Saar, M., and M. Manga. 2004. Depth dependence of permeability in the Oregon Cascades inferred from hydrogeologic, thermal, seismic, and magmatic modeling constraints. *Journal of Geophysical Research: Solid Earth* 109, no. B4: 1–19.

Saetre, P. 2015. The biosphere model for radionuclide transport and dose assessment in SR-PSU, Svensk kärnbränslehantering (SKB) Techinal Report R-13-46.

Sanford, W. 2002. Recharge and groundwater models: An overview. *Hydrogeology Journal* 10, no. 1: 110–120.

Sawyer, A.H., and M.B. Cardenas. 2009. Hyporheic flow and residence time distributions in heterogeneous cross-bedded sediment. *Water Resources Research* 45, no. 8: 1–12.

Schuetz, T., and M. Weiler. 2011. Quantification of localized groundwater inflow into streams using ground-based infrared thermography. *Geophysical Research Letters* 38, no. 3: 1–5.

Selroos, J.O., and S.L. Painter. 2012. Effect of transport-pathway simplifications on projected releases of radionuclides from a nuclear waste repository (Sweden). *Hydrogeology Journal* 20, no. 8: 1467–1481.

Selroos, J.O., D.D. Walker, A. Ström, B. Gylling, and S. Follin. 2002. Comparison of alternative modelling approaches for groundwater flow in fractured rock. *Journal of Hydrology* 257, no. 1–4: 174–188.

Singh, A., V. Phogat, R. Dahiya, and S. Batra. 2014. Impact of long-term zero till wheat on soil physical properties and wheat productivity under rice-wheat cropping system. *Soil and Tillage Research* 140: 98–105.

Song, J., X. Chen, C. Cheng, S. Summerside, and F. Wen. 2007. Effects of hyporheic processes on streambed vertical hydraulic conductivity in three rivers of Nebraska. *Geophysical Research Letters* 34, no. 7: 1–5.

Stanford, J.A., and J. Ward. 1993. An ecosystem perspective of alluvial rivers: Connectivity and the hyporheic corridor. *Journal of the North American Benthological Society* 12, no. 1: 48–60.

Sterte, E.J., E. Johansson, Y. Sjöberg, R.H. Karlsen, and H. Laudon. 2018. Groundwater-surface water interactions across scales in a boreal landscape investigated using a numerical modelling approach. *Journal of Hydrology* 560: 184–201.

Stonedahl, S.H., J.W. Harvey, A. Wörman, M. Salehin, and A.I. Packman. 2010. A multiscale model for integrating hyporheic exchange from ripples to meanders. *Water Resources Research* 46, no. 12: 1–14.

Tonina, D., and J.M. Buffington. 2007. Hyporheic exchange in gravel bed rivers with pool-riffle morphology: Laboratory experiments and three-dimensional modeling. *Water Resources Research* 43, no. 1: 1–16.

Tóth, J. 1963. A theoretical analysis of groundwater flow in small drainage basins. *Journal of Geophysical Research* 68, no. 16: 4795–4812.

Trauth, N., C. Schmidt, M. Vieweg, U. Maier, and J.H. Fleckenstein. 2014. Hyporheic transport and biogeochemical reactions in pool-riffle systems under varying ambient groundwater flow conditions. *Journal of Geophysical Research: Biogeosciences* 119, no. 5: 910–928.

Turcotte, D. 1997. *Fractals and Chaos in Geology and Geophysics*, 2nd ed. New York: Cambridge University, Press.

Vissers, M.J., and M. van der Perk. 2008. The stability of groundwater flow systems in unconfined sandy aquifers in The Netherlands. *Journal of Hydrology* 348, no. 3–4: 292–304.

Wang, J.Z., A. Wörman, E. Bresciani, L. Wan, X.-S. Wang, and X.-W. Jiang. 2016. On the use of late-time peaks of residence time distributions for the characterization of hierarchically nested groundwater flow systems. *Journal of Hydrology* 543: 47–58.

Wang, J.Z., X.-W. Jiang, L. Wan, X.-S. Wang, and H. Li. 2014. An analytical study on groundwater flow in drainage basins with horizontal wells. *Hydrogeology Journal* 22, no. 7: 1625–1638.

Wang, C., J.D. Gomez-Velez, and J.L. Wilson. 2018. The importance of capturing topographic features for modeling groundwater flow and transport in mountainous watersheds. *Water Resources Research* 54, no. 12: 10,313–10,338.

Welch, L.A., D.M. Allen, and H. Van Meerveld. 2012. Topographic controls on deep groundwater contributions to mountain headwater streams and sensitivity to available recharge. *Canadian Water Resources Journal/Revue Canadienne Des Ressources Hydriques* 37, no. 4: 349–371.

Whitaker, S. 1986. Flow in porous media I: A theoretical derivation of Darcy's law. *Transport in Porous Media* 1, no. 1: 3–25.

Wörman, A., J. Riml, B.B. Mojarrad, and S. Xu. 2019. Parameterizing water fluxes in the geosphere-biosphere interface zone: For use in biosphere modelling as part of the long-term safety assessment. 17th International High-Level Radioactive Waste Management Conference, IHLRWM 2019, 14-18, Knoxville, United States.

Wörman, A., L. Marklund, S. Xu, and B. Dverstorp. 2007a. Impact of repository depth on residence times for leaking radionuclides in land-based surface water. *Acta Geophysica* 55, no. 1: 73–84.

Wörman, A., A.I. Packman, L. Marklund, J.W. Harvey, and S.H. Stone. 2007b. Fractal topography and subsurface water flows from fluvial bedforms to the continental shield. *Geophysical Research Letters* 34, no. 7: 1–5.

Wörman, A., A.I. Packman, L. Marklund, J.W. Harvey, and S.H. Stone. 2006. Exact three-dimensional spectral solution to surface-groundwater interactions with arbitrary surface topography. *Geophysical Research Letters* 33, no. 7: 1–4.

Wörman, A., B.A. Dverstorp, R.A. Klos, and S. Xu. 2004. Role of the bio-and geosphere interface on migration pathways for 135Cs and ecological effects. *Nuclear Technology* 148, no. 2: 194–204.

Xu, S., B. Dverstorp, A. Woerman, L. Marklund, R. Klos, and G. Shaw. 2008. SSI's independent consequence calculations in support of the regulatory review of the SR-Can safety assessment. SSI Rapport 2008:08, Statens Strålsyddsinstitut (SSI), Sweden.

Xu, S., and A. Wörman. 1999. Implications of sorption kinetics to radionuclide migration in fractured rock. *Water Resources Research* 35, no. 11: 3429–3440.

Zijl, W. 1999. Scale aspects of groundwater flow and transport systems. *Hydrogeology Journal* 7, no. 1: 139–150.